SCHOOL OF COMPUTATION,
INFORMATION AND TECHNOLOGY

TECHNICAL UNIVERSITY OF MUNICH

Master's Thesis in Computational Science and Engineering

# Wave Reversal in SeisSol using the Instantaneous Time Mirror

Vikas Kurapati


SCHOOL OF COMPUTATION,
INFORMATION AND TECHNOLOGY

TECHNICAL UNIVERSITY OF MUNICH


Master's Thesis in Computational Science and Engineering

# Wave Reversal in SeisSol using the Instantaneous Time Mirror


| | |
|---|---|
| Author: | Vikas Kurapati |
| Supervisor: | Prof. Dr. Michael Bader |
| Advisor: | Lukas Krenz, Sebastian Wolf |
| Submission Date: | October 15, 2023 |


I confirm that this master's thesis is my own work and I have documented all sources and material used.

Garching bei München, October 15, 2023 Vikas Kurapati

# Acknowledgments

I would like to express my deepest gratitude to my supervisor, Prof. Dr. Michael Bader and my advisor, Lukas Krenz for their invaluable guidance, support, and encouragement throughout my master's thesis. Their vast knowledge, constructive criticism, and prompt feedback helped shape my ideas and made this thesis possible.

I would like to thank Prof. Gregor Hillers for giving me the opportunity and welcoming me to Helsinki, Finland to collaborate with the team at University of Helsinki to work and get more ideas to work on my thesis. I would also like to thank Prof. Alice Gabriel for being involved in the project and providing us valuable inputs. The discussions have helped me get ideas on how to go about the thesis and the project in general.

I would also like to thank the faculty members of the Chair of Scientific Computing for their continuous support and for providing me with a challenging yet rewarding academic experience. Their passion and dedication to teaching and research have been a great source of inspiration to me.

I am indebted to my family and friends for their unwavering support, encouragement, and patience during this challenging journey. Their love and faith in me have been my constant motivation.

# Abstract

This thesis presents a numerical investigation of the wave reversal technique using the Instantaneous Time Mirror method in the simulation software SeisSol. Earthquakes produce two different kinds of waves i.e., P- and S-waves. The focus of the study is to develop a novel approach to accurately determine the source of an earthquake by analyzing the time evolution of the seismic waves in both the forward and time-reversed directions. We analyse the application of an Instantaneous Time Mirror (ITM) on a planar travelling wave and spherical waves produced by point sources. We then refocus each of the P- and S-waves separately to the source location. We demonstrate the application of the ITM on different types of point sources and show that the ITM is able to refocus the waves to the source location.

# Contents

# 1 Introduction

Studying seismic phenomena provides valuable insights and potential techniques for identifying areas that are more susceptible to earthquakes, mitigating economic impacts, and reducing casualities.

The field of earthquake simulation has seen significant advancements in recent years, thanks to the availability of powerful supercomputers [Cui+10], [Bre15], [Käs+10]. With these resources, it has become possible to model realistic 3D earthquake events on a large scale, something that was not feasible until a few decades ago. Today's simulation software heavily relies on numerical methods to approximate real-life physics. In this process, the volume of the problem is discretized into smaller elements, and numerical solvers are employed in each element to obstain a solution. A few examples out of these wide range of numerical methods used to solve wave equations are finite differences, finite volumes and finite elements. These numerical methods have played a crucial role in advancing the field of earthquake simulation and are continuously being improved to produce more accurate and efficient simulations.

SeisSol[1] is a scientific software that enables the simulation of seismic waves and earthquake phenomena. However, the modelling of complex 3D geometries can be computationally intensive. To address this challenge, SeisSol implements an efficient way to optimally utilize the computing resources. The software allows for the study of various scenarios, including adjusting material properties to exhibit elastic, viscoelastic and viscoplastic behaviour. SeisSol utilizes a combination of Discontinuous Galerkin (DG) method and Arbitrary high-order schemes using DERivates (ADER) time-integration approach to solve the problems. This combination is called ADER-DG approach [Dum03]. [DK06] extended this approach to solve the elastic wave equations in three dimensions. The ADER-DG approach provides arbitrary high-order accuracy in space and time, with the solution in each element approximated by polynomials. The degrees of freedom are expressed through the coefficients of the polynomial, which are advanced in time during simulation, allowing for discontinuities across element boundaries [KD06].

In this thesis, we extend SeisSol with the implementation of Wave Reversal of Seismic waves using the Instantaneous Time Mirror (ITM). Time-reversal techniques have been researched in the field of acoustic media, primarily in order to focus the wave below the diffraction limit [Fin+89]. This methodology may be applied, for instance, to improve

[1] https://seissol.org

the detection of gallstones within the human body [Fin97]. In the context of seismic waves, time-reversal methods may be employed to investigate the source and origin of the seismic waves. The work by [FF17] describes two techniques for wave reversal. The first approach is the time-reversal mirror approach, which involves recording the wavefield at some receiver locations and reversing the wavefield. This approach has been used experimentally to reverse wavefields in elastic solids [Cat+08]. [Wei16] describes a Loschmidt's demon as something which reverses the momentum/velocity of each particle instantaneously such that the state of the system is reversed from a fibrillated state to a less fibrillated, smoother state. The second approach for wave-reversal is called the Instantaneous Time Mirror (ITM) approach, which involves mimicking Loschmidt's Demons for waves [FF17]. While both techniques generate time-reversed waves, we specifically focus on the ITM approach. This method involves manipulating waves on time boundaries by sudden modifications of the wave properties like wave speed or impedance in the whole medium, effectively mimicking the Loschmidt point of view. This approach is very efficient for radiating time-reversed waves without the use of any antennas or receivers. The first approach, which utilizes "time-reversal mirrors" with wave manipulation along a spatial boundary sampled by a finite number of antennas, has numerous applications in telecommunication, imaging, therapy, and defense [FF17]. [Bac+16] have experimentally demonstrated the instantaneous time mirrors on surface waves on water by manipulating the wave speed for a period of time using a vertical jolt. This is shown to refocus the waves at the source position before diverging again.

To achieve ITMs in a simulation environment, we modify the impedances of seismic waves for a short period of time $t_{ITM}$ to $t_{ITM} + \tau$ by manipulating the material properties $\lambda, \mu, \rho$. As the impedances of seismic waves depend on these three properties, this manipulation is sufficient to achieve wave reversal using ITMs.

It is important to note that the time-reversal presented here, in its simplest form, may not be directly useful in experimental investigations, as we cannot directly modify the material properties. However, it does provide an approach to approximately locate the source of an earthquake when successfully reversed.

The thesis is organized as follows: Chapter 2 focuses on the fundamental theory of elastic wave propagation and the presentation of the numerical ADER-DG scheme as used in SeisSol. The equations of motion in elastic media is derived, and the wave equation is presented in the velocity-stress formulation. Chapter 3 outlines the theory of time-reversal, briefly discussing the wave reversal approach before delving into a more detailed explanation of the ITMs concept. Section 3.4 describes the method and implementation details of ITMs in SeisSol. Chapter 4 discusses the different studies and results obtained in the process for different scenarios. Finally, we discuss the conclusions and possible future research directions in Chapter 5.

# 2 Seismic Waves and ADER-DG formulation

In this chapter, the necessary theoretical foundations for this thesis are established through the derivation of fundamental equations governing the propagation of elastic waves. The equation of motion corresponding to this will be presented later on in the velocity-stress formulation. We only consider isotropic media and utilize this assumption in particular symmtery arguments. The restriction to isotropic media is a commonly employed simplification, as seen in works such as [DK06].

Section 2.2 discusses the fundamental framework of SeisSol, the numerical tool employed for simulating seismic wave phenomena. SeisSol is a combination of the Discontinuous Galerkin Finite Element (DG-FE) method and a time integration scheme based on the solution of ADER, as described in previous works [DK06], [Käs+10]. This approach, known as ADER-DG will be introduced in more detail.

## 2.1 Elastic Wave Equation

An elastic medium is characterized by an undeformed state, in which stresses and strains are zero, to which it will return to in the absence of outer forces. If the stresses and strains the medium experiences are infinitesimal, the theory of linear elasticity applies. We define the displacement vector, $\mathbf{U}$, describing the shortest distance between the initial and current position of a point. The particle velocities $u, v$ and $w$ in $x, y$ and $z$ direction, respectively, can then be defined as the temporal derivative of $\mathbf{U}$

$$\begin{aligned} \frac{\partial U_x}{\partial t} &= \dot{U}_x = u, \\ \frac{\partial U_y}{\partial t} &= \dot{U}_y = v, \\ \frac{\partial U_z}{\partial t} &= \dot{U}_z = w, \end{aligned} \tag{2.1}$$

where the subscript denotes the coordinate direction and a dot over a variable represents its partial time derivative leading to the following notation:

$$\frac{\partial U_i}{\partial t} = \dot{U}_i = V_i, \tag{2.2}$$

where the velocity vector, $\mathbf{V}$, is introduced for convenience. $\mathbf{V} = [V_1, V_2, V_3] = [u, v, w]$ are used analogously.

In the context of linear elasticity, the following extension of Hooke's law to generalize linear elasticity holds

$$\sigma_{ij} = c_{ijkl}\epsilon_{kl}, \tag{2.3}$$

with the medium specific constants $c_{ijkl}$. The Einstein summation convention is followed, where an index appearing twice is summed over all possible values. In this context, $\sigma_{ij}$ represents the stress tensor and $\epsilon_{kl}$ represents the strain tensor. Hooke's law expresses that stress tensor components are linear combinations of strain tensor components. For infinitesimally small perturbations, the strain tensor components $\epsilon_{kl}$ are defined as follows

$$\epsilon_{kl} = \frac{1}{2}\left(\partial_k U_l + \partial_l U_k\right), \tag{2.4}$$

where $\partial_k$ represents the spatial derivative in $k$-direction and $U_i$ represents the displacement in $i$-direction. Previously, we mentioned our focus on the velocity-stress formulation rather than the displacement-stress formulation. To eliminate the displacements $U_i$, we introduced velocities $V_i$ in equation 2.2. Consequently, this leads to the time derivative of the strain tensor

$$\partial_t \epsilon_{kl} = \frac{1}{2}\left(\partial_k V_l + \partial_l V_k\right), \tag{2.5}$$

expressed in terms of the spatial derivatives of the velocities $V_i$. Here, $\partial_t$ denotes the time derivative. As the constants $c_{ijkl}$ remain constant over time,

$$\partial_t \sigma_{ij} = c_{ijkl}\partial_t \epsilon_{kl}. \tag{2.6}$$

We can apply symmetry considerations of the stress tensor i.e., $\sigma_{ij} = \sigma_{ji}$ to the term $c_{ijkl}$ in equation 2.3 and reduce the number of independent components from 81 to 21 [AR02, Cha. 2]. This in turn lets us define the tensor in terms of two constants in isotropic media with the general form of

$$c_{ijkl} = \lambda\delta_{ij}\delta_{kl} + \mu\left(\delta_{ik}\delta_{jl} + \delta_{il}\delta_{jk}\right), \tag{2.7}$$

where $\delta$ is the Kronecker delta function and $\lambda, \mu$ are the Lamé parameters.

We now write a force balance in a volume $V$ within a surface $S$. The momentum within the volume changes at a rate equal to the forces acting on that volume. Therefore, the forces acting on these comprise a body force and a surface force, which result from the presence of normal and shear stresses. This can be written mathematically as

$$\frac{\partial}{\partial t}\int_V \rho\frac{\partial \mathbf{U}}{\partial t}dV = \int_V \mathbf{f}dV + \oint_S \mathbf{T}\left(\mathbf{n}\right)dS, \tag{2.8}$$

where $\frac{\partial}{\partial t}\int_V \rho\frac{\partial \mathbf{U}}{\partial t}dV$, is the momentum of the control volume with density $\rho$, and $\mathbf{T}$ is the traction vector which is related to the stress tensor by Cauchy's stress theorem

$$T_j\left(n\right) = \sigma_{ij}n_i, \tag{2.9}$$

with the normal vector $n_i$. Applying Gauss' divergence theorem

$$\oint_S \mathbf{T}(\mathbf{n}) dS = \oint_S \sigma_{ij} n_i dS = \int_V \partial_j \sigma_{ij} dV, \tag{2.10}$$

Replacing **T** in equation 2.8 using equations 2.9 and 2.10 and reordering the terms gives us

$$\int_V \left( \rho \frac{\partial^2 U_i}{\partial t^2} - f_i - \partial_j \sigma_{ij} \right) dV = 0. \tag{2.11}$$

Here we assumed that the stress tensor is symmetric, i.e., $\sigma_{ij} = \sigma_{ji}$. As it is true for any general volume, we can equate the integrand to zero. This gives us the equation

$$\rho \frac{\partial^2 U_i}{\partial t^2} = f_i + \partial_j \sigma_{ij}. \tag{2.12}$$

Expanding equation 2.12 in $j$ and using $V_i = \frac{\partial U_i}{\partial t}$, we get

$$\rho \frac{\partial V_i}{\partial t} = f_i + \partial_x \sigma_{xi} + \partial_y \sigma_{yi} + \partial_z \sigma_{zi}, \tag{2.13}$$

The body force $f_i$ will be discussed later in terms of the source terms.

Combining equations 2.6, 2.7 and 2.13, we obtain the final 3D wave elastic equation for an isotropic medium in velocity-stress formulation as follows

$$\begin{aligned}
\frac{\partial \sigma_{xx}}{\partial t} - (\lambda + 2\mu) \frac{\partial u}{\partial x} - \lambda \frac{\partial v}{\partial y} - \lambda \frac{\partial w}{\partial z} &= S_1, \\
\frac{\partial \sigma_{yy}}{\partial t} - \lambda \frac{\partial u}{\partial x} - (\lambda + 2\mu) \frac{\partial v}{\partial y} - \lambda \frac{\partial w}{\partial w} &= S_2, \\
\frac{\partial \sigma_{zz}}{\partial t} - \lambda \frac{\partial u}{\partial x} - \lambda \frac{\partial v}{\partial y} - (\lambda + 2\mu) \frac{\partial w}{\partial z} &= S_3, \\
\frac{\partial \sigma_{xy}}{\partial t} - \mu \left( \frac{\partial v}{\partial x} + \frac{\partial u}{\partial y} \right) &= S_4, \\
\frac{\partial \sigma_{yz}}{\partial t} - \mu \left( \frac{\partial v}{\partial z} + \frac{\partial w}{\partial y} \right) &= S_5, \\
\frac{\partial \sigma_{xz}}{\partial t} - \mu \left( \frac{\partial u}{\partial z} + \frac{\partial w}{\partial x} \right) &= S_6, \\
\rho \frac{\partial u}{\partial t} - \frac{\partial \sigma_{xx}}{\partial x} - \frac{\partial \sigma_{xy}}{\partial y} - \frac{\partial \sigma_{xz}}{\partial z} &= \rho S_7, \\
\rho \frac{\partial v}{\partial t} - \frac{\partial \sigma_{xy}}{\partial x} - \frac{\partial \sigma_{yy}}{\partial y} - \frac{\partial \sigma_{yz}}{\partial z} &= \rho S_8, \\
\rho \frac{\partial w}{\partial t} - \frac{\partial \sigma_{xz}}{\partial x} - \frac{\partial \sigma_{yz}}{\partial y} - \frac{\partial \sigma_{zz}}{\partial z} &= \rho S_9,
\end{aligned} \tag{2.14}$$

where $S_p, p = 1, \dots 9$, are the source terms. The source terms are used to describe the common sources of seismic events like double couple or force couple moments. These are often used to approximate the faults and slips in Earth's structure [She19].

Another important term for consideration with this system is the propagation speed of elastic-acoustic waves. In elastic media, we observe two kinds of waves, a primary compression wave and a secondary sheer wave which are called P- and S-waves respectively.

For the investigation of the eigenstructure of the systems, we need to transform it into a more compact form of hyperbolic equations

$$\frac{\partial Q_p}{\partial t} + A_{pq}\frac{\partial Q_q}{\partial x} + B_{pq}\frac{\partial Q_q}{\partial y} + C_{pq}\frac{\partial Q_q}{\partial z} = 0, \tag{2.15}$$

where $\mathbf{Q}$ is the state vector with $p$ unknown variables which contains the stresses and velocities, i.e.,

$$\mathbf{Q} = \left(\sigma_{xx},\, \sigma_{yy},\, \sigma_{zz},\, \sigma_{xy},\, \sigma_{yz},\, \sigma_{xz},\, u,\, v,\, w\right)^T \tag{2.16}$$

and $A_{pq}, B_{pq}, C_{pq}$ are space-dependent flux matrices. Where

$$A_{pq} = \begin{bmatrix} 0 & 0 & 0 & 0 & 0 & 0 & -(\lambda+2\mu) & 0 & 0 \\ 0 & 0 & 0 & 0 & 0 & 0 & -\lambda & 0 & 0 \\ 0 & 0 & 0 & 0 & 0 & 0 & -\lambda & 0 & 0 \\ 0 & 0 & 0 & 0 & 0 & 0 & 0 & -\mu & 0 \\ 0 & 0 & 0 & 0 & 0 & 0 & 0 & 0 & 0 \\ 0 & 0 & 0 & 0 & 0 & 0 & 0 & 0 & -\mu \\ -\frac{1}{\rho} & 0 & 0 & 0 & 0 & 0 & 0 & 0 & 0 \\ 0 & 0 & 0 & -\frac{1}{\rho} & 0 & 0 & 0 & 0 & 0 \\ 0 & 0 & 0 & 0 & 0 & -\frac{1}{\rho} & 0 & 0 & 0 \end{bmatrix}, \tag{2.17}$$

$$B_{pq} = \begin{bmatrix} 0 & 0 & 0 & 0 & 0 & 0 & 0 & -\lambda & 0 \\ 0 & 0 & 0 & 0 & 0 & 0 & 0 & -(\lambda+2\mu) & 0 \\ 0 & 0 & 0 & 0 & 0 & 0 & 0 & -\lambda & 0 \\ 0 & 0 & 0 & 0 & 0 & 0 & -\mu & 0 & 0 \\ 0 & 0 & 0 & 0 & 0 & 0 & 0 & 0 & -\mu \\ 0 & 0 & 0 & 0 & 0 & 0 & 0 & 0 & 0 \\ 0 & 0 & 0 & -\frac{1}{\rho} & 0 & 0 & 0 & 0 & 0 \\ 0 & -\frac{1}{\rho} & 0 & 0 & 0 & 0 & 0 & 0 & 0 \\ 0 & 0 & 0 & 0 & -\frac{1}{\rho} & 0 & 0 & 0 & 0 \end{bmatrix}, \tag{2.18}$$

$$C_{pq} = \begin{bmatrix} 0 & 0 & 0 & 0 & 0 & 0 & 0 & 0 & -\lambda \\ 0 & 0 & 0 & 0 & 0 & 0 & 0 & 0 & -\lambda \\ 0 & 0 & 0 & 0 & 0 & 0 & 0 & 0 & -(\lambda + 2\mu) \\ 0 & 0 & 0 & 0 & 0 & 0 & 0 & 0 & 0 \\ 0 & 0 & 0 & 0 & 0 & 0 & 0 & -\mu & 0 \\ 0 & 0 & 0 & 0 & 0 & 0 & -\mu & 0 & 0 \\ 0 & 0 & 0 & 0 & 0 & -\frac{1}{\rho} & 0 & 0 & 0 \\ 0 & 0 & 0 & 0 & -\frac{1}{\rho} & 0 & 0 & 0 & 0 \\ 0 & 0 & -\frac{1}{\rho} & 0 & 0 & 0 & 0 & 0 & 0 \end{bmatrix}, \tag{2.19}$$

The eigenvalues of the flux matrices $A_{pq}, B_{pq}, C_{pq}$ determine the propagation velocities of elastic waves. These velocities can be expressed as

$$s_1 = -v_p,\ s_2 = -v_s,\ s_3 = -v_s,\ s_4 = 0,\ s_5 = 0,\ s_6 = 0,\ s_7 = v_s,\ s_8 = v_s,\ s_9 = v_p, \tag{2.20}$$

where

$$v_p = \sqrt{\frac{\lambda + 2\mu}{\rho}}, \quad v_s = \sqrt{\frac{\mu}{\rho}}. \tag{2.21}$$

These two velocities are the propagation velocities with $v_p$ as the propagation velocity of the P-wave and $v_s$ as the propagation velocity of the S-wave.

The elastic wave propagation is simplified to an acoustic wave propagation when we set $\mu = 0$. Further simplifications like

$$\sigma_{ij} = 0, \forall i \neq j \tag{2.22}$$

can be derived from the set of equations 2.14. All the diagonal elements $\sigma_{ii} = \lambda \partial_j u_j$ are equal to each other which is analogous to the physical pressure in acoustic media.

$$-p = \sigma_{xx} = \sigma_{yy} = \sigma_{zz}. \tag{2.23}$$

This condenses the equations of motion as

$$\begin{aligned} \frac{\partial p}{\partial t} + \lambda \frac{\partial u}{\partial x} + \lambda \frac{\partial v}{\partial y} + \lambda \frac{\partial w}{\partial z} &= S_1, \\ \rho \frac{\partial u}{\partial t} + \frac{\partial p}{\partial x} &= \rho S_2, \\ \rho \frac{\partial v}{\partial t} + \frac{\partial p}{\partial y} &= \rho S_3, \\ \rho \frac{\partial w}{\partial t} + \frac{\partial p}{\partial z} &= \rho S_4. \end{aligned} \tag{2.24}$$

When equation 2.24 is written in the form of equation 2.15, we get

$$A_{pq} = \begin{bmatrix} 0 & \lambda & 0 & 0 \\ \frac{1}{\rho} & 0 & 0 & 0 \\ 0 & 0 & 0 & 0 \\ 0 & 0 & 0 & 0 \end{bmatrix}, \tag{2.25}$$

$$B_{pq} = \begin{bmatrix} 0 & 0 & \lambda & 0 \\ 0 & 0 & 0 & 0 \\ \frac{1}{\rho} & 0 & 0 & 0 \\ 0 & 0 & 0 & 0 \end{bmatrix}, \tag{2.26}$$

$$C_{pq} = \begin{bmatrix} 0 & 0 & 0 & \lambda \\ 0 & 0 & 0 & 0 \\ 0 & 0 & 0 & 0 \\ \frac{1}{\rho} & 0 & 0 & 0 \end{bmatrix}, \tag{2.27}$$

with eigenvalues

$$s_1 = -v_p,\ s_2 = 0,\ s_3 = 0,\ s_4 = v_p\,, \tag{2.28}$$

with

$$v_p = \sqrt{\frac{\lambda}{\rho}}. \tag{2.29}$$

This shows that there is only kind of propagating wave in the acoustic case with $\mu = 0$.

## 2.2 ADER-DG

In this section, we outline the fundamental framework of SeisSol. Our aim is provide a concise understanding of the framework avoiding excessive detail.

### 2.2.1 Discontinuous Galerkin Method

We have earlier formulated the elastic wave equation as a system of linear hyperbolic Partial Differential Equation (PDE)s in equation 2.14. [TMN01] formulated the idea of arbitrary high order generalized Riemann Solvers in a finite volume framework and coined the approach ADER. Here, the combination of the generalized Riemann Solvers with DG methods is explained, resulting in ADER-DG approach [DM06]. In practice, we use a time-averaged normal Riemann problem where we first predict the solution in time and then solve a Riemann problem making it in practice a time-averaged Riemann problem which is equivalent to the generalized Riemann solver.

Higher-order piecewise polynomial approximations are used along with the theory of fluxes across element boundaries from the finite volume methods. The ADER-DG scheme is an explicit one step scheme. It advances the solution by a full time step and needs the computation of inter-cell fluxes once per timestep.

To solve the 3D elastic wave equation with the ADER-DG method, we use the compact form as in equation 2.15. We use an unstructured mesh and thus divide our computational domain $\Omega \in \mathbb{R}^3$ into tetrahedral elements $\mathcal{T}^{(m)}$, with unique indices $m \in \mathbb{N}$.

$A_{pq}, B_{pq}, C_{pq}$ are assumed to be piecewise constant. We now introduce a new coordinate system of $(\xi, \eta, \zeta)$ with the frame of reference as a tetrahedron as shown in figure 2.1

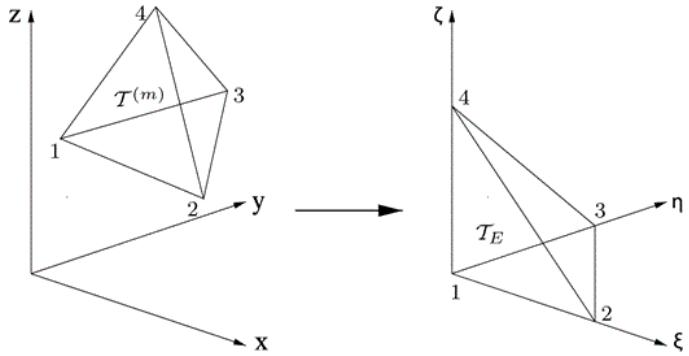


Figure 2.1: Transforming tetrahedron into a reference frame.(Figure taken from Figure 1 in [DK06])

As we are dealing with a new transformed coordinate system, we would need a Transformation matrix to transform the vector $Q_p$ from the global Cartesian system to the vector $Q_q^n$ in the normal, face-aligned frame. The transformation would be of the form

$$Q_p = T_{pq} Q_q^n. \tag{2.30}$$

[DK06] calculates the transformation matrix $T_{pq}$ as

$$T_{pq} = \begin{bmatrix} n_x^2 & s_x^2 & t_x^2 & 2n_x s_x & 2s_x t_x & 2n_x t_x & 0 & 0 & 0 \\ n_y^2 & s_y^2 & t_y^2 & 2n_y s_y & 2s_y t_y & 2n_y t_y & 0 & 0 & 0 \\ n_z^2 & s_z^2 & t_z^2 & 2n_z s_z & 2s_z t_z & 2n_z t_z & 0 & 0 & 0 \\ n_y n_x & s_y s_x & t_y t_x & n_y s_x + n_x s_y & s_y t_x + s_x t_y & n_y t_x + n_x t_y & 0 & 0 & 0 \\ n_z n_y & s_z s_y & t_z t_y & n_z s_y + n_y s_z & s_z t_y + s_y t_z & n_z t_y + n_y t_z & 0 & 0 & 0 \\ n_z n_x & s_z s_x & t_z t_x & n_z s_x + n_x s_z & s_z t_x + s_x t_z & n_z t_x + n_x t_z & 0 & 0 & 0 \\ 0 & 0 & 0 & 0 & 0 & 0 & n_x & s_x & t_x \\ 0 & 0 & 0 & 0 & 0 & 0 & n_y & s_y & t_y \\ 0 & 0 & 0 & 0 & 0 & 0 & n_z & s_z & t_z \end{bmatrix}, \tag{2.31}$$

where $\mathbf{n} = \left(n_x, n_y, n_z\right)^T$ are the components of the normal vector, and $\mathbf{s} = \left(s_x, s_y, s_z\right)^T$ and $\mathbf{t} = \left(t_x, t_y, t_z\right)^T$ are the tangential vectors of the boundary face of the tetrahedron. $\mathbf{n}, \mathbf{s}, \mathbf{t}$ are orthogonal to each other. To represent the numerical solution $Q_h$ as a linear combination of pure space-dependent but time-independent polynomial basis functions with time-dependent coeeficients, we introduce the time-dependent degrees of freedom $\hat{Q}_m(t)$.

$$Q_p^{(m)}(x, y, z, t) = \hat{Q}_{pl}^{(m)}(t) \Psi_l(x, y, z), \tag{2.32}$$

where $\Psi_l(x,y,z)$ are spatial polynomial basis functions defined on the physical element. As it is more practical to define the polynomial basis functions on the reference element so that we can pre-calculate the integrals, we express equation 2.32 in the frame of the reference element using a suitable coordinate transformation M which maps the physical coordinates $(x,y,z)$ with the reference element $(\xi,\eta,\zeta)$

$$Q_p^{(m)}(x,y,z,t) = \hat{Q}_{pl}^{(m)}(t)\,\Psi_l(M(x,y,z)). \tag{2.33}$$

This formulation allows us to define the polynomial basis functions on the reference element $\Phi_l(\xi,\eta,\zeta)$. As we can compute the integrals in the reference system beforehand, the coordinate transformation makes our implementation more computationally efficient. This allows us to express $Q_h$ in each tetrahedron after the transformation of the coordinates as

$$\left[Q_H^{(m)}\right]_p(\xi,\eta,\zeta,t) = \hat{Q}_{pl}^{m}(t)\,\Phi_l(\xi,\eta.\zeta), \tag{2.34}$$

where $l$ denotes the $l^{th}$ basis function. Multiplying equation 2.15 with the test function $\Phi_k$ [CKS11] and integrating over our tetrahedral element $\mathcal{T}^{(m)}$ gives

$$\int_{\mathcal{T}^{(m)}} \Phi_k \frac{\partial Q_p}{\partial t} dV + \int_{\mathcal{T}^{(m)}} \Phi_k \left( A_{pq}\frac{\partial Q_q}{\partial x} + B_{pq}\frac{\partial Q_q}{\partial y} + C_{pq}\frac{\partial Q_q}{\partial z}\right) dV = 0. \tag{2.35}$$

We add fluxes $F_p^h$ at the boundaries of the tetrahedron to equation 2.35 to include discontinuities in $Q_h$ and we integrate by parts to obtain the weak form as

$$\int_{\mathcal{T}^{(m)}} \Phi_k \frac{\partial Q_p}{\partial t} dV + \int_{\partial\mathcal{T}^{(m)}} F_p^h dS - \int_{\mathcal{T}^{(m)}} \left( \frac{\partial \Phi_k}{\partial x} A_{pq}Q_q + \frac{\partial \Phi_k}{\partial y} B_{pq}Q_q + \frac{\partial \Phi_k}{\partial z} C_{pq}Q_q \right) dV = 0. \tag{2.36}$$

The flux between the tetrahedron $\mathcal{T}^{(m)}$ with the boundary extrapolated numerical solution $\hat{Q}_{sl}\Phi_l^{(m)}$ and one of its neighboring tetrahedra $\mathcal{T}^{(m_j)}$ $(j=1,2,3,4)$ is computed in the global, coordinate system using the flux matrix $A_{pq}$ from equation 2.17

$$\begin{aligned} F_p^h = &\frac{1}{2} T_{pq} \left( A_{qr}^{(m)} + \left| A_{qr}^{(m)} \right| \right) (T_{rs})^{-1} \hat{Q}_{sl}^{(m)} \Phi_l^{(m)} \\ &+ \frac{1}{2} T_{pq} \left( A_{qr}^{(m)} - \left| A_{qr}^{(m)} \right| \right) (T_{rs})^{-1} \hat{Q}_{sl}^{(m_j)} \Phi_l^{(m_j)}, \end{aligned} \tag{2.37}$$

where

$$\left| A_{qr}^{(m)} \right| = R_{qp}^{A} \left| \Lambda_{ps} \right| (R_{sr})^{-1}, \tag{2.38}$$

and $\Lambda$ is a diagonal matrix with eigenvalues of $A_{pq}$ and $R_{pq}$ is a matrix with right eigenvectors of $A_{pq}$ stacked in columns. The next step is inserting fluxes from equation 2.37 and $Q_h$ from equation 2.34 into the weak formulation in equation 2.36. But as the

basis functions $\Phi_l$ are defined on $(\xi, \eta, \zeta)$, we need to transform the resulting equation with the transformation

$$\mathrm{d}x\,\mathrm{d}y\,\mathrm{d}z = |J|\,\mathrm{d}\xi\,\mathrm{d}\eta\,\mathrm{d}\zeta, \tag{2.39}$$

where $|J|$ is the determinant of the Jacobian matrix of the coordinate transformation and linear combination of the flux matrices to create transformed flux matrices

$$\begin{aligned} A^*_{pq} &= A_{pq}\frac{\partial \xi}{\partial x} + B_{pq}\frac{\partial \xi}{\partial y} + C_{pq}\frac{\partial \xi}{\partial z}, \\ B^*_{pq} &= A_{pq}\frac{\partial \eta}{\partial x} + B_{pq}\frac{\partial \eta}{\partial y} + C_{pq}\frac{\partial \eta}{\partial z}, \\ C^*_{pq} &= A_{pq}\frac{\partial \zeta}{\partial x} + B_{pq}\frac{\partial \zeta}{\partial y} + C_{pq}\frac{\partial \zeta}{\partial z}. \end{aligned} \tag{2.40}$$

We finally get the semi-discrete DG formulation of the ODE system within the reference tetrahedron $\mathcal{T}_E$

$$\begin{aligned} &\frac{\partial \hat{Q}^{(m)}_{pl}}{\partial t}\,|J| \int_{\mathcal{T}_E} \Phi_k \Phi_l d\xi d\eta d\zeta \\ &+ \sum_{j=1}^{4} T^j_{pq}\frac{1}{2}\left(A^{(m)}_{qr} + \left|A^{(m)}_{qr}\right|\right)\left(T^j_{rs}\right)^{-1}\hat{Q}^{(m)}_{sl}\,|S_j|\,F^{-,j}_{kl} \\ &+ \sum_{j=1}^{4} T^j_{pq}\frac{1}{2}\left(A^{(m)}_{qr} - \left|A^{(m)}_{qr}\right|\right)\left(T^j_{rs}\right)^{-1}\hat{Q}^{(m_j)}_{sl}\,|S_j|\,F^{+,j,i,h}_{kl} \\ &- A^*_{pq}\hat{Q}^{(m)}_{ql}\,|J| \int_{\mathcal{T}_E} \frac{\partial \Phi_k}{\partial \xi}\Phi_l d\xi d\eta d\zeta \\ &- B^*_{pq}\hat{Q}^{(m)}_{ql}\,|J| \int_{\mathcal{T}_E} \frac{\partial \Phi_k}{\partial \eta}\Phi_l d\xi d\eta d\zeta \\ &- C^*_{pq}\hat{Q}^{(m)}_{ql}\,|J| \int_{\mathcal{T}_E} \frac{\partial \Phi_k}{\partial \zeta}\Phi_l d\xi d\eta d\zeta = 0, \end{aligned} \tag{2.41}$$

where

$$\begin{aligned} F^{-,j}_{kl} &= \int_{\partial(\mathcal{T}_E)_j} \Phi_k\left(\xi^{(j)}(\chi,\tau)\right)\Phi_l\left(\xi^{(j)}(\chi,\tau)\right)d\chi d\tau, \quad \forall 1 \le j \le 4, \\ F^{+,j,i,h}_{kl} &= \int_{\partial(\mathcal{T}_E)_j} \Phi_k\left(\xi^{(j)}(\chi,\tau)\right)\Phi_l\left(\xi^{(i)}\left(\tilde{\chi}^{(h)}(\chi,\tau), \tilde{\tau}^{(h)}(\chi,\tau)\right)\right)d\chi d\tau, \quad \forall 1 \le i \le 4, \quad 1 \le h \le 3. \end{aligned} \tag{2.42}$$

$F^{-,j}_{kl}$ accounts for the contribution of the element$(m)$ itself to the fluxes over face j and $F^{+,j,i,h}_{kl}$ accounts for the contribution of the element's direct side neighbor$\left(k_j\right)$ to the fluxes over the face $j$ and $\left|S_j\right|$ is the area of the face $j$ of the tetrahedron [DK06].

We have not considered the source terms in the final formulation given in equation 2.41. The source terms are dealt with as presented in [KMD07].

### 2.2.2 ADER Time Discretization

Instead of now utilizing the Runge-Kutta method to derive a limited fourth-order in time Runge-Kutta DG scheme, we adopt the ADER approach to achieve an arbitrary high-order accuracy in both spatial and temporal dimensions. Runge-Kutta schemes of order higher than 4 tend to become inefficient as the number of calculation steps required exceeds the order of accuracy due to the Butcher barriers [But87].

By applying the ADER scheme to the DG formulation described in equation 2.41, we obtain the ADER-DG scheme. The crucial step in this approach involves using the Cauchy-Kovalewski procedure to replace time-derivatives with pure space derivatives. As a consequence, the Cauchy-Kovalewski procedure provides the $k^{th}$ time-derivative as shown in equation 2.43 in the face-aligned coordinate system, allowing us to achieve higher accuracy without the limitations of tradiational Runge-Kutta schemes

$$\frac{\partial^k Q_p}{\partial t^k} = (-1)^k \left( A^*_{pq} \frac{\partial}{\partial \xi} + B^*_{pq} \frac{\partial}{\partial \eta} + C^*_{pq} \frac{\partial}{\partial \zeta} \right)^k Q_q. \tag{2.43}$$

$Q_p$ can be expanded in a Taylor series with respect to time, and then the time derivatives can be substituted with space derivatives using the equation 2.43 [DK06, Sec. 3.2]. By adopting this approach, we can achieve arbitrary high-order accuracy in both spatial and temporal dimensions. As previously mentioned, the ADER-DG schemes conduct time integration within a single time step, considering only the current element and its neighboring elements, making it well-suited for parallelization. Moreover, studies have demonstrated that the ADER-DG method outperforms traditional schemes such as Runge Kutta Discontinuous Galerkin (RK-DG) scheme [DM05].

### 2.2.3 Boundary Conditions

Up until now, we have explored the time-discretization and space-discretization aspects of our problem. To complete our numerical solver, we must establish suitable boundary conditions for the problem. We mainly have two kinds of boundaries in consideration.

#### Absorbing Boundaries

With the implementation of absorbing boundary conditions, the physical volume is enclosed by such boundaries in the forward direction. This means that no waves enter the computational domain, and any outgoing waves smoothly pass through the boundary without experiencing reflection. A careful examination of equation 2.37 reveals that its first term on the right-hand side corresponds to the outflow from the current element, while the second term represents the inflow from neighboring elements. To prevent incoming waves from affecting the solution, we set the second term to zero. Consequently, the flux at all absorbing faces of the respective tetrahedral elements is then appropriately set to

$$F_p^{AbsorbBC} = \frac{1}{2} T_{pq} \left( A_{qr}^{(m)} + \left| A_{qr}^{(m)} \right| \right) \left( T_{rs} \right)^{-1} \hat{Q}_{sl}^{(m)} \Phi_l^{(m)}. \tag{2.44}$$

**Free-Surface Boundaries**

At a free-surface boundary, the elastic medium is in contact with the surrounding air or void. In this scenario, there are no external forces acting on the outside of the elastic medium. To ensure that normal and shear stresses vanish at the free surface, a technique involving ghost cells is employed. These ghost cells are used to mirror the stresses, such that their values have the same magnitude as the actual stresses but with the opposite sign. This approach effectively satisfies the condition of stress equilibrium at the free surface, allowing for an accurate treatment at the boundary. We implement this using the flux function [DK06]

$$\begin{aligned} F_p^{FreeBC} = & \frac{1}{2} T_{pq} \left( A_{qr}^{(m)} + \left| A_{qr}^{(m)} \right| \right) \left( T_{rs} \right)^{-1} \hat{Q}_{sl}^{(m)} \Phi_l^{(m)} \\ & + \frac{1}{2} T_{pq} \left( A_{qr}^{(m)} - \left| A_{qr}^{(m)} \right| \right) \Gamma_{rs} \left( T_{st} \right)^{-1} \hat{Q}_{tl}^{(m)} \Phi_l^{(m)}, \end{aligned} \tag{2.45}$$

where $\Gamma_{rs} = diag\left(-1, 1, 1, -1, 1, -1, 1, 1, 1\right)$ is the matrix which mirrors the normal and shear stresses.

## 2.3 Summary

In this chapter we have discussed the governing equations of linear elasticity as a sytem of hyperbolic PDEs. We then discussed the ADER-DG method for numerically solving this system of equations. We have also looked at the boundary conditions that we will use in our numerical solver.

# 3 Time Reversal

Time-reversal methods involve mirroring the propagation of waves in time, aiming to converge the resulting wave back to its source. [FF17] mentions two ways to achieve time-reversal. The first method involves Time Reversal Mirror (TRM)s, which rely on Cauchy boundary conditions. If the wavefield and its normal derivative are known at the entire surface $S$ surrounding the volume $V$ at all times $t$, the wavefield inside the entire volume can be computed. In this approach, the outgoing wave is initially recorded on $S$, then time-reversed and finally emitted from $S$.

Alternatively, time-reversal can be achieved with manipulation of the initial conditions. In this case, the wavefield and its normal derivative are known inside the entire volume but only for a specific time. [Wei16] describes Loschmidt's demon as something hypothetical which reverses the momentum/velocity of each particle instantaneously such that the state of the system is reversed from a fibrillated state to a less fibrillated, smoother state. By emulating Loschmidt's demons [Wei16], which act on the whole space simultaneously, it is possible to instantly reverse the velocity of each particle [FF17]. This leads to the creation of a time-reversed wave. This approach is commonly referred to as the Instantaneous Time Mirror (ITM).

This thesis primarily focuses on the ITM approach for seismic waves. In this method, a time-reversed wave is generated through a sudden modification of the wave propagation properties of the medium [Bac+16]. Section 3.1 delves into the theoretical foundation behind the ITM, providing a comprehensive understanding of its principles. In the latter part of the chapter, we present the implementation of ITM within the numerical simulation software SeisSol. The description of the implementation is kept as general as possible, allowing for a broad grasp of the method's application and utility.

## 3.1 Theory of Instantaneous Time Mirrors

Time-reversal methods for waves are based on the time-reversal invariance of wave equations. They rely on the fact that any wave-field can be completely determined within a volume by knowing the field(and its normal derivative) on any enclosing surface [Bac+16]. We write the elastic wave equation in its second order vector form [AR02, Cha. 2] as

$$\rho\ddot{\mathbf{U}}\left(\mathbf{x},t\right)-\left(\lambda+2\mu\right)\nabla\left(\nabla\cdot\mathbf{U}\left(\mathbf{x}.t\right)\right)+\mu\nabla\times\left(\nabla\times\mathbf{U}\left(\mathbf{x},t\right)\right)=\mathbf{S}\left(\mathbf{x},t\right), \tag{3.1}$$

with the source function $\mathbf{S}\left(\mathbf{x},t\right)$. This implies that if $\hat{\mathbf{U}}\left(\mathbf{x},t\right)$ is a solution, then $\hat{\mathbf{U}}\left(\mathbf{x},-t\right)$ is also a solution, if $\mathbf{S}$ is symmetric in time such that $\mathbf{S}\left(\mathbf{x},t\right)=\mathbf{S}\left(\mathbf{x},-t\right)$.

The ITM approach is closely connected to the Cauchy theorem, which states that the wave field evolution can be deduced from the knowledge of the wave field and its derivative at one single time, i.e., the initial conditions. By inducing a sudden modification of the wave propagation properties(such as impedance) in the medium, we change the initial conditions at two different instances creating a time-reversed wave. This modification, referred to as the ITM, does not require the use of antennas or the entire wave field's memory [Bac+16]. [Bac+16] demonstrated this for water waves with physical and numerical experiments resulting in successful refocusing of the generated waves into their sources' shapes. This was achieved by introducing a temporal slab in the wave velocities as shown in figure 3.1.

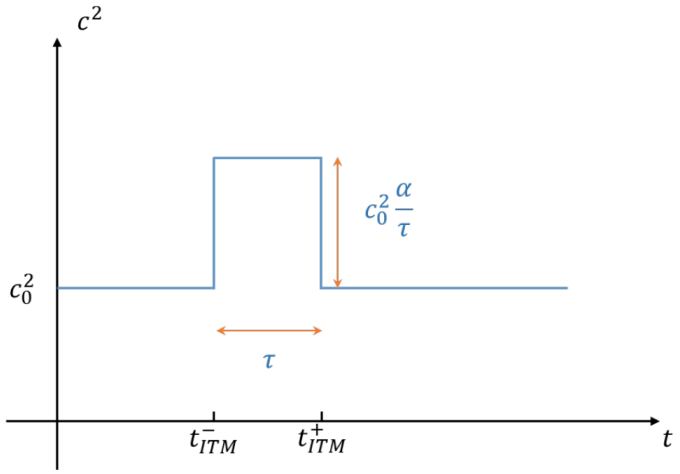


Figure 3.1: Rectangular profile for the wave velocity. Properties of the wave are changed during the duration of ITM. (Figure taken from Figure 1 in [Bac+16, Supplementary Material])

In the context of elastic waves, as we have seen in equations 2.14 and 2.21, there are two propagating waves, i.e., P- and S-waves. [LeV02, Sec 9.6-Sec 9.8] shows that in case of spacial material interfaces, a discontinuity in the quantity called Impedance $Z = \rho v$ causes reflections across the material interface. [KL05, Eq. 1.66 and 1.180] show that impedances of P- and S-waves are defined analogously as $Z_p = \rho v_p$ and $Z_s = \rho v_s$.

## 3.2 ITM on a one-dimensional acoustic planar wave

In this section, we calculate the analytical solution for a one-dimensional acoustic wave when an ITM is applied from $t_{ITM}^-$ to $t_{ITM}^+$. For this, we consider a one-dimensional acoustic equation [LeV02, Sec. 2.8] linearized about the motionless state

$$\begin{aligned} p_t + K_0 u_x &= 0, \\ u_t + \frac{1}{\rho_0} p_x &= 0, \end{aligned} \tag{3.2}$$

where $p$ is the pressure perturbation, $K_0$ is the bulk modulus of the material and $u$ is the velocity perturbation. This can be written in consolidated matrix vector form as done for first order hyperbolic systems of equations as follows

$$\frac{\partial}{\partial t}\begin{bmatrix} p \\ u \end{bmatrix} + \begin{bmatrix} 0 & K_0 \\ \frac{1}{\rho_0} & 0 \end{bmatrix} \frac{\partial}{\partial x}\begin{bmatrix} p \\ u \end{bmatrix} = 0. \tag{3.3}$$

The flux matrix of equation 3.3 has two eigenvalues

$$\lambda_1 = -c_0, \quad \lambda_2 = c_0, \tag{3.4}$$

where

$$c_0 = \sqrt{\frac{K_0}{\rho_0}} \tag{3.5}$$

is the speed of sound. Waves can propagate in either direction with this speed. The eigenvectors for this coefficient matrix are

$$r^1 = \begin{bmatrix} -\rho_0 c_0 \\ 1 \end{bmatrix}, \quad r^2 = \begin{bmatrix} \rho_0 c_0 \\ 1 \end{bmatrix}. \tag{3.6}$$

The impedance as mentioned in section 3.1 is defined as

$$Z_0 = \rho_0 c_0. \tag{3.7}$$

Using these parameters, [LeV02, Sec. 2.8] calculates the solution of the acoustic equation depending on the initial conditions $p^0(x), u^0(x)$ as:

$$\begin{aligned} p(x,t) &= \frac{1}{2}\left[p^0\left(x + c_0 t\right) + p^0\left(x - c_0 t\right)\right] - \frac{Z_0}{2}\left[u^0\left(x + c_0 t\right) - u^0\left(x - c_0 t\right)\right], \\ u(x,t) &= -\frac{1}{2Z_0}\left[p^0\left(x + c_0 t\right) - p^0\left(x - c_0 t\right)\right] + \frac{1}{2}\left[u^0\left(x + c_0 t\right) + u^0\left(x - c_0 t\right)\right]. \end{aligned} \tag{3.8}$$

We use this solution to find the analytical solution of a 1D acoustic wave after the ITM is applied in two different ways. First we ensure we use initial conditions which give rise to only one forward wave. We simply use a sinusoidal wave multiplied with one eigenvector $r^2$. This defines our initial conditions as

$$\begin{aligned} p^0(x) &= \rho_0 c_0 \cos(kx), \\ u^0(x) &= \cos(kx), \end{aligned} \tag{3.9}$$

where $k$ is the wave number of the wave. To ensure that our domain is periodic, we defined our domain to be between two wavelengths, i.e., from $\left[-\frac{\pi}{k}, \frac{\pi}{k}\right]$. The energy of the system is defined in this domain as [KGN21]

$$E_1 = \int_{-\frac{\pi}{k}}^{\frac{\pi}{k}} \left(\frac{1}{2K}p^2 + \frac{1}{2}\rho u^2\right) dx, \tag{3.10}$$

which simplifies to

$$E_1 = \frac{\pi\rho_0}{k}, \tag{3.11}$$

for phase 1. Energy defined in equation 3.10 is conserved for a particular phase as the system of equations are conservative for every phase [KGN21].

### 3.2.1 Impedance Changing ITM

Using the conditions given by equation 3.9, we calculate the solution at $t^-_{ITM}$ and use them as initial conditions for the new equation where the material properties are changed. In this case, we modify the material properties such that the velocities are scaled while the impedance also changes. This is achieved by modifying the bulk modulus while keeping the density constant. Using 3.8, we get the initial conditions for the next phase of the simulation$\left(t^-_{ITM} \leq t \leq t^+_{ITM}\right)$ at $t^-_{ITM}$ as

$$\begin{aligned} p^0_{t^-_{ITM}}(x) &= c_0\rho_0 \cos\left(kx - c_0 k t^-_{ITM}\right), \\ u^0_{t^-_{ITM}}(x) &= \cos\left(kx - c_0 k t^-_{ITM}\right). \end{aligned} \tag{3.12}$$

We now use these initial conditions and equation 3.8 with the updated wave velocity and constant density to get the evolved solution for $t^-_{ITM} \leq t \leq t^+_{ITM}$. We used [The] to perform the arithmetic simplifications. We obtain the solution for this period as

$$\begin{aligned} p_2(x,t) &= -\frac{1}{2}(n-1)\, c_0\rho_0 \cos\left(kx + c_0 knt - (c_0 kn + c_0 k)\, t^-_{ITM}\right) \\ &\quad + \frac{1}{2}(n+1)\, c_0\rho_0 \cos\left(kx - c_0 knt + (c_0 kn - c_0 k)\, t^-_{ITM}\right), \\ u_2(x,t) &= \frac{1}{2}(n-1) \cos\left(kx + c_0 knt - (c_0 kn + c_0 k)\, t^-_{ITM}\right) \\ &\quad + \frac{1}{2}(n+1) \cos\left(kx - c_0 knt + (c_0 kn - c_0 k)\, t^-_{ITM}\right), \end{aligned} \tag{3.13}$$

where n is the velocity scaling factor. We now use these expressions to calculate the energy as we have already done in equation 3.10. This gives us the energy in the second phase, i.e., $t^-_{ITM} \leq t \leq t^+_{ITM}$ to be

$$E_2 = \frac{1}{2}\frac{\left(1+n^2\right)\pi\rho_0}{kn^2}. \tag{3.14}$$

This shows that the energy drops when the velocity is scaled up. We then check the relative drop in energy for different scaling factors and see that it asymptotes to 0.5 for higher scaling factors. The variation of the ratio with the scaling factor can be seen in figure 3.2.

Now, the velocity is scaled back to its initial value at $t = t^+_{ITM}$. By defining $\tau = t^+_{ITM} - t^-_{ITM}$, a similar calculation is performed to acquire the solution for the final phase,

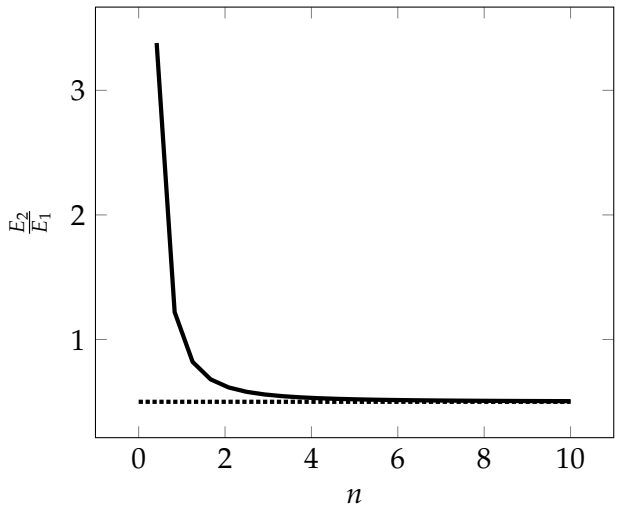


Figure 3.2: Relative Energy $\left(\frac{E_2}{E_1}\right)$ in $t^{-}_{ITM} \leq t \leq t^{+}_{ITM}$.

i.e., $t \geq t^{+}_{ITM}$, and the resulting solution is

$$
\begin{aligned}
p_3(x,t) = & -\frac{\frac{1}{4}c_0\rho_0\left(-n^2+1\right)\cos\left(kx+c_0kt-2\,c_0kt^{-}_{ITM}-(c_0kn+c_0k)\tau\right)}{n} \\
& -\frac{\frac{1}{4}c_0\rho_0\left(n^2-1\right)\cos\left(kx+c_0kt-2\,c_0kt^{-}_{ITM}+(c_0kn-c_0k)\tau\right)}{n} \\
& -\frac{\frac{1}{4}c_0\rho_0\left(n^2-2n+1\right)\cos\left(kx-c_0kt+(c_0kn+c_0k)\tau\right)}{n} \\
& -\frac{\frac{1}{4}c_0\rho_0\left(-n^2-2n-1\right)\cos\left(kx-c_0kt-(c_0kn-c_0k)\tau\right)}{n}, \\
u_3(x,t) = & -\frac{\frac{1}{4}\left(n^2-1\right)\cos\left(kx+c_0kt-2\,c_0kt^{-}_{ITM}-(c_0kn+c_0k)\tau\right)}{n} \\
& -\frac{\frac{1}{4}\left(-n^2+1\right)\cos\left(kx+c_0kt-2\,c_0kt^{-}_{ITM}+(c_0kn-c_0k)\tau\right)}{n} \\
& -\frac{\frac{1}{4}\left(n^2-2n+1\right)\cos\left(kx-c_0kt+(c_0kn+c_0k)\tau\right)}{n} \\
& -\frac{\frac{1}{4}\left(-n^2-2n-1\right)\cos\left(kx-c_0kt-(c_0kn-c_0k)\tau\right)}{n}.
\end{aligned}
\tag{3.15}
$$

Using these quantities, we now calculate the energy using the equation 3.10

$$
E_3 = -\pi\rho_0\frac{\left(1+n^4-2\,n^2\right)\cos^2\left(c_0kn\tau\right)-\left(1+n^4\right)}{2\,kn^2}. \tag{3.16}
$$

The final energy $E_3$ is dependent on the parameters: $k, n, \tau$ and is bounded as

$$
\frac{\pi\rho_0}{K} \leq E_3 \leq \frac{\pi\rho_0}{2K}\left[n^2+\frac{1}{n^2}\right]. \tag{3.17}
$$

This demonstrates that the application of ITM leads to a change in the energy of our system. We compare the worst case scenario, i.e., what would be the maximum energy increase after the ITM is applied. For that, we take the upper bound and plot the ratio $\frac{E_3}{E_1}$ with $n$ as we did before in figure 3.3.

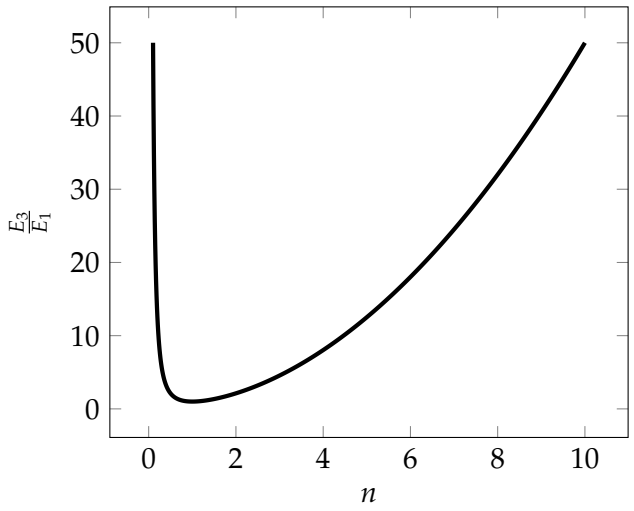


Figure 3.3: Maximum Relative Energy $\left(\frac{E_3}{E_1}\right)$ in $t \geq t^+_{ITM}$

The minimum value for this energy jump lies at $n = 1$, which means no velocity scaling and no reflections. This particular scenario does not offer any practical utility or relevance to our objective.

### 3.2.2 Constant Impedance ITM

We know that there is no reflected wave in space interfaces when the impedance stays constant [LeV02, Sec 9.7]. Here, we test out the same with a time interface, i.e., we perform ITM such that the velocities scale but the impedance stays constant. This is achieved by scaling the wave speed by $n$ and the density by $\frac{1}{n}$. Similar to section 3.2.1, we choose the initial conditions as

$$\begin{aligned} p^0(x) &= Z_0 \cos(kx), \\ u^0(x) &= \cos(kx). \end{aligned} \tag{3.18}$$

Using these parameters, the energy is once again computed as in equation 3.10 and is found to be

$$E_1 = \frac{\pi Z_0}{c_0 k}. \tag{3.19}$$

Using the conditions given in equation 3.18, we calculate the solution at $t^-_{ITM}$ and use them as initial conditions for the new equation where the wave velocities are scaled. In this case, we scale the velocities such that the impedance does not change. This is

achieved by scaling the density down. Using 3.8, we get the initial conditions for the next phase of the simulation$\left(t_{ITM}^{-} \leq t \leq t_{ITM}^{+}\right)$ at $t_{ITM}^{-}$ as

$$\begin{aligned} p^{0}_{t_{ITM}^{-}}(x) &= Z_0 \cos\left(kx - c_0 k t_{ITM}^{-}\right), \\ u^{0}_{t_{ITM}^{-}}(x) &= \cos\left(kx - c_0 k t_{ITM}^{-}\right). \end{aligned} \tag{3.20}$$

We now use these as the initial conditions and equation 3.8 with the updated wave velocity and constant density to get the evolved solution for $t_{ITM}^{-} \leq t \leq t_{ITM}^{+}$. We used [The] to perform the simplifications for the arithmetic. We obtain the solution for this period as

$$\begin{aligned} p_2(x,t) &= Z_0 \cos\left(kx - c_0 knt + (c_0 kn - c_0 k) t_{ITM}^{-}\right), \\ u_2(x,t) &= \cos\left(kx - c_0 knt + (c_0 kn - c_0 k) t_{ITM}^{-}\right), \end{aligned} \tag{3.21}$$

where n is the velocity scaling factor. We now use these expressions to calculate the energy using equation 3.10. This gives us the energy in the second phase, i.e., $t_{ITM}^{-} \leq t \leq t_{ITM}^{+}$ to be

$$E_2 = \frac{\pi z_0}{c_0 kn}. \tag{3.22}$$

We obverse that there is no extra reflected wave and the wave speed is just increased with a phase shift and that the energy is directly scaled down by the velocity scaling factor.

Now, the velocity is scaled down again to its original value at $t = t_{ITM}^{+}$ and defining $\tau = t_{ITM}^{+} - t_{ITM}^{-}$, we do a similar calculation to obtain the solution for the final phase, i.e., $t \geq t_{ITM}^{+}$ as

$$\begin{aligned} p_3(x,t) &= Z_0 \cos\left(kx - c_0 kt - (c_0 kn - c_0 k)\tau\right), \\ u_3(x,t) &= \cos\left(kx - c_0 kt - (c_0 kn - c_0 k)\tau\right). \end{aligned} \tag{3.23}$$

Using these quantities, we now calculate the energy using equation 3.10

$$E_3 = \frac{\pi Z_0}{c_0 k}, \tag{3.24}$$

which is equal to $E_1$. This shows that there is no final energy increase when the impedance is kept constant. The final solution also has no reflected wave and has the same wave speed as the initial wave and has a phase shift in time. This confirms that even in time interfaces, similar to space interfaces there is no reflection.

## 3.3 ITM on a 3D acoustic planar wave

In this section, we calculate the analytical solution for a 3D Acoustic wave when an ITM is applied from $t_{ITM}^{-}$ to $t_{ITM}^{+}$.

To do this, we consider a three dimensional acoustic equation linearised over the stationary state, where $p$ is the pressure perturbation, $K_0$ is the bulk modulus of the material and $u$, $v$, $w$ are the velocity perturbations in $x$, $y$, $z$ respectively. This can be written in consolidated matrix vector form as done for first order hyperbolic systems of equations as

$$\frac{\partial}{\partial t}\mathbf{q} + \mathbf{A}\frac{\partial}{\partial x}\mathbf{q} + \mathbf{B}\frac{\partial}{\partial y}\mathbf{q} + \mathbf{C}\frac{\partial}{\partial z}\mathbf{q} = 0, \tag{3.25}$$

where

$$\mathbf{q} = \begin{bmatrix} p \\ u \\ v \\ w \end{bmatrix}, \quad \mathbf{A} = \begin{bmatrix} 0 & K_0 & 0 & 0 \\ \frac{1}{\rho_0} & 0 & 0 & 0 \\ 0 & 0 & 0 & 0 \\ 0 & 0 & 0 & 0 \end{bmatrix}, \quad \mathbf{B} = \begin{bmatrix} 0 & 0 & K_0 & 0 \\ 0 & 0 & 0 & 0 \\ \frac{1}{\rho_0} & 0 & 0 & 0 \\ 0 & 0 & 0 & 0 \end{bmatrix}, \quad \mathbf{C} = \begin{bmatrix} 0 & 0 & 0 & K_0 \\ 0 & 0 & 0 & 0 \\ 0 & 0 & 0 & 0 \\ \frac{1}{\rho_0} & 0 & 0 & 0 \end{bmatrix}. \tag{3.26}$$

We assume an ansatz of

$$\mathbf{q}(\mathbf{x}, t) = \mathbf{q_0} \cos(\mathbf{k} \cdot \mathbf{x} - \omega t), \tag{3.27}$$

where $\mathbf{k} = (k_1, k_2, k_3)$ is the wave number of the planar wave. Using the derivatives of equation 3.25,

$$\begin{aligned} \frac{\partial \mathbf{q}}{\partial t} &= \omega \mathbf{q_0} \sin(\mathbf{k} \cdot \mathbf{x} - \omega t), \\ \frac{\partial \mathbf{q}}{\partial x} &= -k_1 \mathbf{q_0} \sin(\mathbf{k} \cdot \mathbf{x} - \omega t), \\ \frac{\partial \mathbf{q}}{\partial y} &= -k_2 \mathbf{q_0} \sin(\mathbf{k} \cdot \mathbf{x} - \omega t), \\ \frac{\partial \mathbf{q}}{\partial z} &= -k_3 \mathbf{q_0} \sin(\mathbf{k} \cdot \mathbf{x} - \omega t). \end{aligned} \tag{3.28}$$

Substituting these back in the equation we get

$$(\omega - \mathbf{A}k_1 - \mathbf{B}k_2 - \mathbf{C}k_3)\, \mathbf{q_0} \sin(\mathbf{k} \cdot \mathbf{x} - \omega t) = 0. \tag{3.29}$$

Dividing by $\sin(\mathbf{k} \cdot \mathbf{x} - \omega t)$ and rearranging the terms, we get

$$(\mathbf{A}k_1 + \mathbf{B}k_2 + \mathbf{C}k_3)\, \mathbf{q_0} = \omega \mathbf{q_0}. \tag{3.30}$$

This shows that $\omega$ is an eigenvalue of $\hat{\mathbf{A}} = \mathbf{A}k_1 + \mathbf{B}k_2 + \mathbf{C}k_3$ and $\mathbf{q_0}$ is an eigenvector. The modified matrix $\hat{\mathbf{A}}$ would then be

$$\hat{\mathbf{A}} = \begin{pmatrix} 0 & K_0 k_1 & K_0 k_2 & K_0 k_3 \\ \frac{k_1}{\rho_0} & 0 & 0 & 0 \\ \frac{k_2}{\rho_0} & 0 & 0 & 0 \\ \frac{k_3}{\rho_0} & 0 & 0 & 0 \end{pmatrix}, \tag{3.31}$$

with the set of eigenvalues after replacing $\sqrt{\frac{K_0}{\rho_0}}$ with $c$

$$\omega_1 = -c\sqrt{k_1^2+k_2^2+k_3^2}, \quad \omega_2 = 0, \quad \omega_3 = 0, \quad \omega_4 = c\sqrt{k_1^2+k_2^2+k_3^2}, \tag{3.32}$$

and the eigenvectors after replacing $\rho_0\sqrt{\frac{K_0}{\rho_0}}$ with $Z_0$,

$$\mathbf{r_1} = \begin{bmatrix} 1 \\ -\frac{k_1}{Z_0\sqrt{k_1^2+k_2^2+k_3^2}} \\ -\frac{k_2}{Z_0\sqrt{k_1^2+k_2^2+k_3^2}} \\ -\frac{k_3}{Z_0\sqrt{k_1^2+k_2^2+k_3^2}} \end{bmatrix}, \quad \mathbf{r_2} = \begin{bmatrix} 0 \\ 1 \\ 0 \\ -\frac{k_1}{k_3} \end{bmatrix}, \quad \mathbf{r_3} = \begin{bmatrix} 0 \\ 0 \\ 1 \\ -\frac{k_2}{k_3} \end{bmatrix}, \quad \mathbf{r_4} = \begin{bmatrix} 1 \\ \frac{k_1}{Z_0\sqrt{k_1^2+k_2^2+k_3^2}} \\ \frac{k_2}{Z_0\sqrt{k_1^2+k_2^2+k_3^2}} \\ \frac{k_3}{Z_0\sqrt{k_1^2+k_2^2+k_3^2}} \end{bmatrix}. \tag{3.33}$$

For the sake of simplicity, we choose $(k_1, k_2, k_3) = (k, 0, 0)$ inducing our wave to travelling along the x-axis. This makes our eigenvalues

$$\omega_1 = -kc, \quad \omega_2 = 0, \quad \omega_3 = 0, \quad \omega_4 = kc. \tag{3.34}$$

We get our eigenvectors as

$$\mathbf{r_1} = \begin{bmatrix} 1 \\ -\frac{1}{Z_0} \\ 0 \\ 0 \end{bmatrix}, \quad \mathbf{r_2} = \begin{bmatrix} 0 \\ 0 \\ 0 \\ 1 \end{bmatrix}, \quad \mathbf{r_3} = \begin{bmatrix} 0 \\ 0 \\ 1 \\ 0 \end{bmatrix}, \quad \mathbf{r_4} = \begin{bmatrix} 1 \\ \frac{1}{Z_0} \\ 0 \\ 0 \end{bmatrix}. \tag{3.35}$$

We pick an initial condition that enforces that the wave travels in only one direction at $t = 0$ i.e.,

$$\mathbf{q_1}(\mathbf{x}, t) = \begin{bmatrix} 1 \\ \frac{1}{Z_0} \\ 0 \\ 0 \end{bmatrix} \cos(kx - kct). \tag{3.36}$$

This wave form satifies our PDE in equation 3.25.

Now, applying ITM in phase 2 leads to a modified $\hat{\mathbf{A}}$, as we make specific changes to our material properties, specifically replacing $K_0$ with $n^2K_0$. The modified matrix would then be

$$\hat{\mathbf{A}}_\mathbf{2} = \begin{bmatrix} 0 & K_0n^2 & 0 & 0 \\ \frac{1}{\rho_0} & 0 & 0 & 0 \\ 0 & 0 & 0 & 0 \\ 0 & 0 & 0 & 0 \end{bmatrix}, \tag{3.37}$$

with eigenvalues

$$\omega_1^2 = -nkc, \quad \omega_2^2 = 0, \quad \omega_3^2 = 0, \quad \omega_4^2 = nkc, \tag{3.38}$$

and eigenvectors

$$\mathbf{r_1^2} = \begin{bmatrix} 1 \\ -\frac{1}{nZ_0} \\ 0 \\ 0 \end{bmatrix}, \quad \mathbf{r_2^2} = \begin{bmatrix} 0 \\ 0 \\ 0 \\ 1 \end{bmatrix}, \quad \mathbf{r_3^2} = \begin{bmatrix} 0 \\ 0 \\ 1 \\ 0 \end{bmatrix}, \quad \mathbf{r_4^2} = \begin{bmatrix} 1 \\ \frac{1}{nZ_0} \\ 0 \\ 0 \end{bmatrix}. \tag{3.39}$$

At $t = t_{ITM}^-$, the solution is

$$\mathbf{q}\left(\mathbf{x}, t_{ITM}^-\right) = \begin{bmatrix} 1 \\ \frac{1}{Z_0} \\ 0 \\ 0 \end{bmatrix} \cos\left(kx - kct_{ITM}^-\right). \tag{3.40}$$

We use this solution as the initial condition for the next phase with the modified PDE. We split this into a linear sum of the eigenvectors of the new flux matrix as

$$\mathbf{q_1}\left(\mathbf{x}, t_{ITM}^-\right) = \alpha_1^2\mathbf{r_1^2} + \alpha_2^2\mathbf{r_2^2} + \alpha_3^2\mathbf{r_3^2} + \alpha_4^2\mathbf{r_4^2}, \tag{3.41}$$

with

$$\begin{aligned} \alpha_1^2 &= \frac{1}{2}\cos\left(kx - kct_{ITM}^-\right)(1-n), \\ \alpha_2^2 &= 0, \\ \alpha_3^2 &= 0, \\ \alpha_4^2 &= \frac{1}{2}\cos\left(kx - kct_{ITM}^-\right)(1+n). \end{aligned} \tag{3.42}$$

[LeV02, Sec 18.5] states that the solution for a linear hyperbolic system with an eigenvector $\hat{\mathbf{q}}$ and an initial condition $\mathbf{q_0} = \hat{\mathbf{q}} f(\mathbf{n}\cdot\mathbf{x})$ and eigenvalues of the system would be $q(\mathbf{x}, t) = \hat{\mathbf{q}} f(\mathbf{n}\cdot\mathbf{x} - st)$. Using initial conditions from equation 3.40 and the linear combindation of the eigenvectors, we get the solution for the second phase as

$$\begin{aligned} \mathbf{q_2}(\mathbf{x}, t) = &\frac{1}{2}\begin{bmatrix} 1 \\ -\frac{1}{nZ_0} \\ 0 \\ 0 \end{bmatrix}(1-n)\cos\left(kx + nkc\left(t - t_{ITM}^-\right) - kct_{ITM}^-\right) \\ &+ \frac{1}{2}\begin{bmatrix} 1 \\ \frac{1}{nZ_0} \\ 0 \\ 0 \end{bmatrix}(1+n)\cos\left(kx - nkc\left(t - t_{ITM}^-\right) - kct_{ITM}^-\right). \end{aligned} \tag{3.43}$$

We define the duration of ITM as $\tau = t^+_{ITM} - t^-_{ITM}$, this makes the initial conditions for our final phase as

$$\begin{aligned}\mathbf{q_2}\left(\mathbf{x}, t^+_{ITM}\right) = \frac{1}{2}\begin{bmatrix}1\\ -\frac{1}{nZ_0}\\ 0\\ 0\end{bmatrix}(1-n)\cos\left(kx + nkc\tau - kct^-_{ITM}\right)\\ + \frac{1}{2}\begin{bmatrix}1\\ \frac{1}{nZ_0}\\ 0\\ 0\end{bmatrix}(1+n)\cos\left(kx - nkc\tau - kct^-_{ITM}\right).\end{aligned} \tag{3.44}$$

The flux matrix, eigenvalues and eigenvectors of the final phase are identical to those of the first phase. We use the initial conditions in equation 3.44 and split the initial conditions into a linear sum of the eigenvectors of the flux matrix similar to what we have done in equation 3.41. We get the new coefficients for this phase as

$$\begin{aligned}\frac{2n}{n^2-1}\alpha^3_1(kx) &= \cos(kx)\sin(kn\tau c)\sin\left(kt^-_{ITM}c\right) - \cos\left(kt^-_{ITM}c\right)\sin(kn\tau c)\sin(kx),\\ \alpha^3_2 &= 0,\\ \alpha^3_3 &= 0,\\ 2n\alpha^3_4(kx) &= \left(2\,n\cos(kn\tau c)\cos\left(kt^-_{ITM}c\right) - \left(n^2+1\right)\sin(kn\tau c)\sin\left(kt^-_{ITM}c\right)\right)\cos(kx)\\ &\quad + \left(\left(n^2+1\right)\cos\left(kt^-_{ITM}c\right)\sin(kn\tau c) + 2\,n\cos(kn\tau c)\sin\left(kt^-_{ITM}c\right)\right)\sin(kx).\end{aligned} \tag{3.45}$$

The final solution for the third phase is then given by

$$\mathbf{q_2}(\mathbf{x}, t) = \begin{bmatrix}1\\ -\frac{1}{Z_0}\\ 0\\ 0\end{bmatrix}\alpha^3_1\left(kx + kc\left(t - t^+_{ITM}\right)\right) + \begin{bmatrix}1\\ \frac{1}{Z_0}\\ 0\\ 0\end{bmatrix}\alpha^3_4\left(kx - kc\left(t - t^+_{ITM}\right)\right). \tag{3.46}$$

This shows that the final wave solution obtained after ITM has both a forward and a backward going component. This is similar to the solution obtained in section 3.2.1.

## 3.4 Implementation

This section outlines the extension incorporated into SeisSol required for the implementation of ITM. The implemenetation has been designed in a generic way, ensuring that the current code can be easily reused for future experiments.

In order to create a time-reversed wave, the material properties of the medium must be altered as described in the previous sections. This can be accomplished via modifications to the Lamé parameters and density from $t^-_{ITM}$ to $t^+_{ITM}$ that correspond

with the intended reflection. As previously discussed, an alteration to the impedance is required to guarantee the presence of a reflected wave component [LeV02, Sec 9.8]. Consequently, we will present various techniques for achieving this impedance change.

### 3.4.1 Reflecting both P- and S-waves by changing their velocities

The first approach is to change the velocities of both P- and S-waves. This is accomplished by modifying the Lamé parameters $\lambda$ and $\mu$ from $t_{ITM}^{-}$ to $t_{ITM}^{+}$ as

$$\begin{aligned} \hat{\lambda} &= n^2\lambda, \\ \hat{\mu} &= n^2\mu, \\ \hat{\rho} &= \rho. \end{aligned} \tag{3.47}$$

This changes the velocities and impedances of both the waves during the duration of the ITM as

$$\begin{aligned} \hat{v}_p &= nv_p, \\ \hat{v}_s &= nv_s, \\ \hat{Z}_p &= nZ_p, \\ \hat{Z}_s &= nZ_s. \end{aligned} \tag{3.48}$$

where $\hat{v}_p, \hat{v}_s, \hat{Z}_p, \hat{Z}_s$ are the velocities and impedances of the P- and S-waves during the ITM duration and $v_p, v_s, Z_p, Z_s$ are the velocities and impedances of the P- and S-waves outside of the ITM duration.

### 3.4.2 Reflecting both P- and S-waves by keeping their velocities constant

Here, we keep the velocities of both P- and S-waves constant but yet change their impedance by manipulating density along with the Lamè parameters. This is achieved by the following manipulation of the material properties

$$\begin{aligned} \hat{\lambda} &= n\lambda, \\ \hat{\mu} &= n\mu, \\ \hat{\rho} &= \frac{\rho}{n}. \end{aligned} \tag{3.49}$$

This changes the impedances of both the waves during the duration of the ITM as

$$\begin{aligned} \hat{v}_p &= v_p, \\ \hat{v}_s &= v_s, \\ \hat{Z}_p &= nZ_p, \\ \hat{Z}_s &= nZ_s. \end{aligned} \tag{3.50}$$

### 3.4.3 Reflecting only P-wave

This is achieved by changing the Lamé parameter $\lambda$ and keeping $\mu$ constant from $t_{ITM}^{-}$ to $t_{ITM}^{+}$

$$\begin{aligned} \hat{\lambda} &= n\lambda, \\ \hat{\mu} &= \mu, \\ \hat{\rho} &= \rho. \end{aligned} \tag{3.51}$$

The scaling of velocities and impedances of the P-wave in this case are not straightforward

$$\begin{aligned} \hat{v}_p &= \sqrt{\frac{\hat{\lambda} + 2\mu}{\rho}}, \\ \hat{Z}_p &= \sqrt{\rho\left(\hat{\lambda} + 2\mu\right)}, \\ \hat{v}_s &= v_s, \\ \hat{Z}_s &= Z_s. \end{aligned} \tag{3.52}$$

Although the specific scaling relationship is not clear, as observed in previous cases, it is evident that there is a difference in impedance of P-wave during ITM, resulting in its reflected component whilst leaving the S-wave unaffected.

### 3.4.4 Reflecting only S-wave

Ensuring that the impedance of S-wave changes while not affecting the P-wave's impedance is essential for reflecting only S-waves. This is the trickiest reflection we try to achieve. The solution to this is not unique but the one that worked for us the best is

$$\begin{aligned} \hat{\lambda} &= \frac{\lambda + 2\mu}{n} - 2n\mu, \\ \hat{\mu} &= n\mu, \\ \hat{\rho} &= n\rho. \end{aligned} \tag{3.53}$$

The scaling of velocities and impedances of both the waves in this case are

$$\begin{aligned} \hat{v}_p &= \frac{v_p}{n}, \\ \hat{Z}_p &= Z_p, \\ \hat{v}_s &= v_s, \\ \hat{Z}_s &= nZ_s. \end{aligned} \tag{3.54}$$

This case is a demonstration where the speed of the wave changes and yet, there will be no reflection of the wave in time as the impedance is constant. Similarly, for the S-wave, even though there is no change in the wave speed, the change of impedance causes the reflection of the wave in time.

### 3.4.5 Time Step Size

Courant-Friedrichs-Lewy (CFL) condition is generally used to limit the maximum time step of an element for explicit time integration schemes. These are influenced by the order of convergence, occuring wave speeds and size of the considered element.

SeisSol uses Local Time Stepping (LTS) schemes for explicit time-stepping. The LTS scheme uses different time steps for different elements in our mesh. SeisSol clustures the elements to reduce the heterogeneity of the LTS algorithm. The clusters summarize the elements in the computational domain advancing with a common time step. We need to modify this common time step of all the clusters accordingly when the material properties are changed as this modification changes the speeds of propagation of the waves. For more details on LTS schemes, interested readers are referred to [Bre15], [DKT07], [CKT09], [Rie+15], [Sen+14], [GLM08], [WK14], [Sch+09].

If the cluster $i$ has the time step $dt_i$, this is how the time step is modified for the ITM duration in different cases

#### Reflecting both the P- and S-waves by changing their velocities or reflecting just the P-wave

In this case, we just need to scale down the time step by the same factor as the velocities of the waves. So, the time step for the cluster $i$ is scaled as

$$\hat{dt}_i = \frac{dt_i}{n}, \tag{3.55}$$

where $\hat{dt}_i$ is the time step of cluster $i$ during the ITM duration.

Here, we notice that in case of reflecting just the P- wave, we still scale by the factor $n$ even though the velocity is not exactly scaled by $n$. This is to maintain simplicity in the code as the scaling of the velocities of just the P-wave is not straightforward. Nevertheless, CFL condition is still satisfied with this scaling.

#### Reflecting both the P- and S-waves by keeping their velocities constant

In this case, we do not need to scale down the time step by the factor $n$ as the velocity is not scaled here but only the impedance of the waves. So, the time step for the clusters are unchanged in this scenario.

$$\hat{dt}_i = dt_i. \tag{3.56}$$

#### Reflecting only the S-wave

Here, we need to scale up the time step by the factor $n$ as the velocity of the P-wave is scaled down by the factor $n$ to ensure that the simulation still follows CFL condition in case of a scaling factor less than 1, i.e., $n < 1$. So, the time step for the cluster $i$ is scaled as

$$\hat{dt}_i = n\, dt_i. \tag{3.57}$$

### 3.4.6 Summary of the Implementation

The implementation of ITM in SeisSol is done in a generic way such that it can be used for any of the above mentioned scenarios. Material modifications for ITM for different scenarios are discussed and the corresponding time step size modifications to keep the simulation stable are also presented. Material modifications are done such that the impedance of only the wave(s) we intend to reflect is changed. The time step size is modified such that the CFL condition is satisfied for every phase of the simulation.

## 3.5 Summary

In this chapter we have discussed the theory of time reversal in the context of seismic waves. We have looked at how an ITM affects a travelling acoustic wave in one dimension and three dimensions. We concluded that we need a shift in impedance rather than velocity of the wave to have a time reflection. We then discussed the implementation of the ITM method in SeisSol.

# 4 Results and Discussion

This chapter presents and analyses the results obtained from applying the ITM on seismic waves. We begin by examining the travelling planar wave before addressing point sources. As a starting point, the time-reversal is analysed in an acoustic media with an initial condition as a travelling planar P-Wave in section 4.1. The second part deals with the time-reversal of a velocity impulse point source in an acoustic medium. The third part deals with the time-reversal of a velocity impulse point source in an elastic medium with refocusing of both P- and S-waves together and separately in sections 4.2 to 4.5. In sections 4.6 and 4.7, we demostrate the application of ITM in reversing waves generated by moment tensors. In all the cases, we check if the refocused wave will converge to the location of the source with the same speed as the original wave. We analyse all cases with a homogenous medium to deliver on a sound proof of concept of the ITM being useful to refocus different kind of waves. We used a modification of our benchmark test problem, WP2-LOH1 to show refocusing in realistic media.
To wrap up, we perform a convergence test to check the correctness of our ITM implementation with the analytical solutions derived in section 3.3.

## 4.1 Time-reversal of a travelling planar P-wave

The acoustic case is a simplification of propagation in an elastic medium. The second Lamé parameter $\mu$ is set to zero. The medium is characterized by

$$\rho = 4, \quad \mu = 0, \quad \lambda = 1. \tag{4.1}$$

The propagation speed of the P-wave in this case is given by

$$v_p = \sqrt{\frac{\lambda + 2\mu}{\rho}} = \sqrt{\frac{1}{4}} = \frac{1}{2}. \tag{4.2}$$

We impose an initial condition such that there is a P-Wave travelling towards the negative x-axis. The details on how the initial conditions are set up to ensure a left going P-wave is discussed in Travelling Wave: SeisSol[1]. We impose a P-Wave with a wavelength of $\lambda = 1.0$. This gives us a timeperiod of $T = 2.0$. We choose a cubic computational domain of [-1, 1] in all three directions with periodic boundary conditions with the triangular mesh shown in figure 4.1 which contains 163840 triangular elements.

[1] https://seissol.readthedocs.io/en/latest/initial-condition.html#travelling-wave

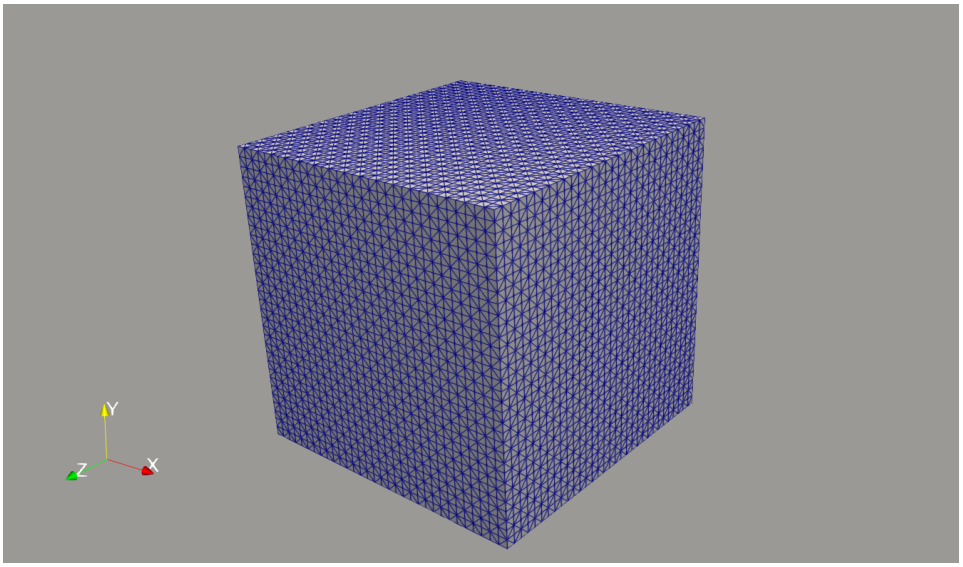


Figure 4.1: Mesh used for the simulation of a travelling planar wave in acoustic medium with ITM

We start our initial travelling wave at the origin and our wave travels to the boundary in $t = \frac{1}{2}$. We start our ITM at $t = 2$ such that the reversed wave will travel back to the origin at $t = 4.0$ to meet the forward going wave.

Figure 4.2 shows the evolution of the wavefield in time. We notice that there is a reflection of the forward going wave and it meets the forward going wave at the origin at $t = 4.0$. This is a proof of concept that the ITM can be used to refocus waves in an acoustic media.

To observe the refocusing in a clearer way, we choose a slice perpendicular to the $z$-axis at the origin and plot the wavefield in terms of $u$-velocity along the $x$-axis at different times in figure 4.3. We can see that at $t = 2.0$, there is a reflected component along with the forward component. At $t = 3.0$, i.e., half the time-period after the application of the ITM, the reflected component interacts with the forward wave for the first time. This shows that in half the time-period, the reflected wave travelled half the wave length interacting with the forward travelling wave. At $t = 4.0$, the reflected wave has travelled the entire wave length and is refocused at the origin.

## 4.2 Time-reversal of wave created by a velocity impulse point source in acoustic media

We now consider a velocity impulse point source in an acoustic medium. We pick the Lamé parameter $\lambda$, density $\rho$ from the half-space of the benchmark case WP2-LOH1[1] to

[1]https://seissol.readthedocs.io/en/latest/pointsource.html

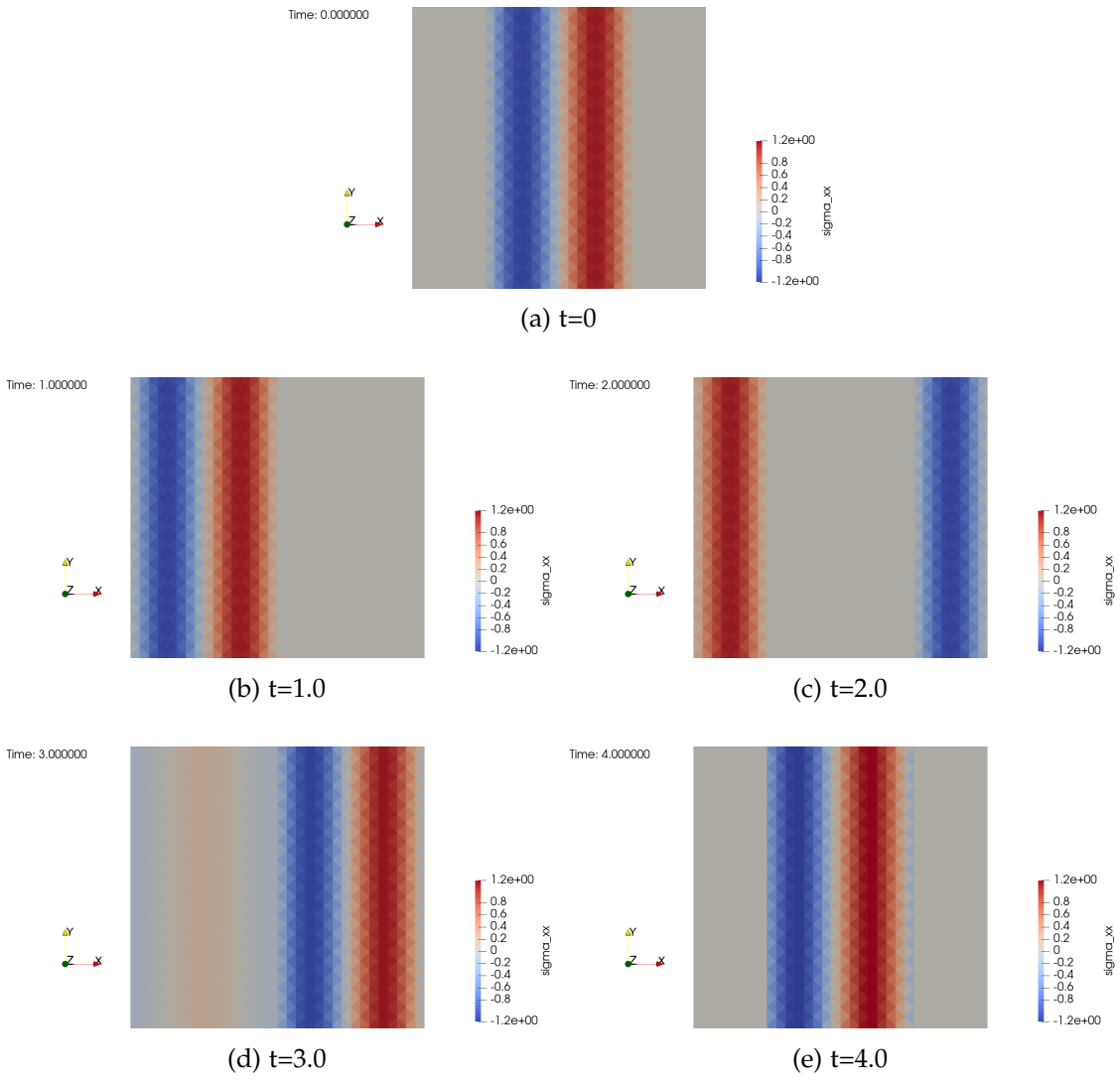


(a) t=0

(b) t=1.0

(c) t=2.0

(d) t=3.0

(e) t=4.0

Figure 4.2: ITM applied on a travelling planar wave in an acoustic media.

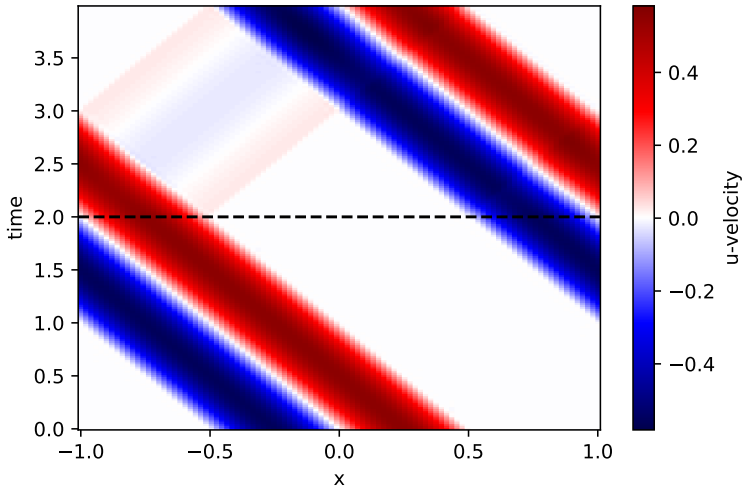


Figure 4.3: Space-time plot for Acoustic Travelling Wave with ITM. We take a slice perpendicular to the $z$-axis at the origin and plot the $u$-velocity along the $x$-axis at different times.

make it a homogenous acoustic medium. The medium is characterized by

$$\begin{aligned} \rho &= 2700.0, \\ \mu &= 0.0, \\ \lambda &= 3.24038016 \cdot 10^{10}. \end{aligned} \tag{4.3}$$

This makes the velocity of the P-wave to be

$$v_p = \sqrt{\frac{3.24038016 \cdot 10^{10}}{2700}} \approx 3464. \tag{4.4}$$

We choose a computational domain of $[-26000, 32000] \times [-26000, 32000] \times [0, 34000]$ and a simulation time of $t = 10.0$ with ITM applied at $t = 5.0$ such that the originating waves do not reflect back from the boundaries at the $x$- and $y$-axis ensuring that reflections due to ITM are clearly noticeable. Our velocity impulse source is at $(3000, 3000, 17000)$, the center of the domain. We have used an unstructured tetrahedral mesh with around 1.4 million elements. We have used more refinement in the region close to the source to capture the steep gradients as in figure 4.4.

The source term is given as

$$\begin{aligned} \dot{S} &= \frac{1}{T^2} t e^{-\frac{t}{T}}, \\ S_i &= \dot{S} \times C_i, \end{aligned} \tag{4.5}$$

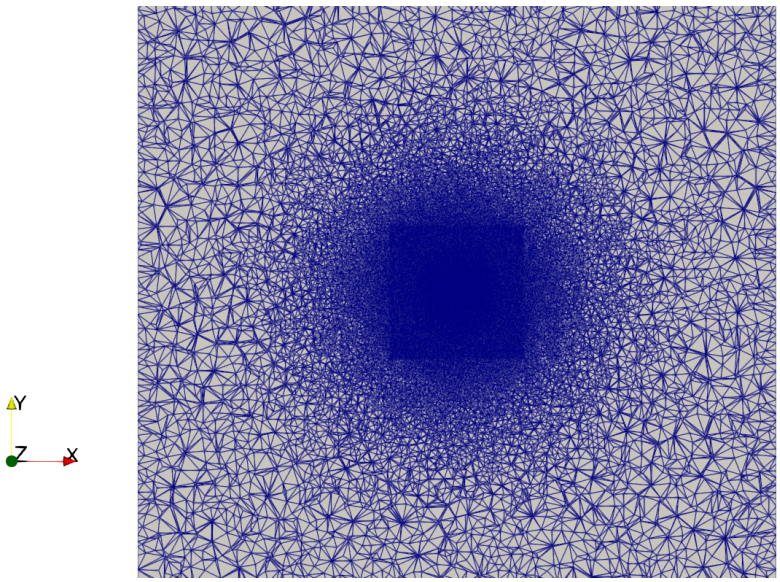


Figure 4.4: Example mesh for simulations with a point source acting as a velocity pulse. We have a finer mesh near the source and a coarser mesh away from the source.

where T is a constant to decide the duration of the source approximately. This source is then applied to equations 7 to 9 in equation 2.14 as per the direction $i$. $i$ is the direction of the source. $i = 7$ is a source applied in $x$-direction, $i = 8$ is a source applied in $y$-direction and $i = 9$ is a source applied in $z$-direction.

We choose T=0.1 and the source to be in the $z$-direction with $C_7 = 0, C_8 = 0, C_9 = 1.2 \cdot 10^{16}$. With this, our source looks like in figure 4.5

We pick a slice at $(3000, 3000, 20000)$, i.e., 3000 away from the source location in $z$-direction. We plot the $u$-velocities along the $x$-axis at different times on this slice. With this setup and velocity impulse, we see that the velocity in $x$-direction looks like in figure 4.6.

We notice that we have only one wave propagating in time as expected as we have an acoustic medium and it reaches our slice around $t = 1.5$. We have observed an unexpected stationary velocity in the vicinity of the source, which requires a thorough investigation with SeisSol. But it does not affect our refocusing and has nothing to do with our application of ITM. We now apply ITM on the same setup at $t = 5.0$. The wavefield looks like in figure 4.7.

We notice that there is a reflected wave travelling back to the source which leaves our slice around $t = 8.5$, showing that the reflected wave is reflected along the line $t = 5.0$, which is our point in time when we applied the ITM. In figure 4.7b, we plot the expected location of the wave front from the forward going and reflected waves assuming that they are spherical waves and they have equal speeds but in opposite directions. It is clear that the reflected wavefronts coincide with the expected locations of the wavefronts.

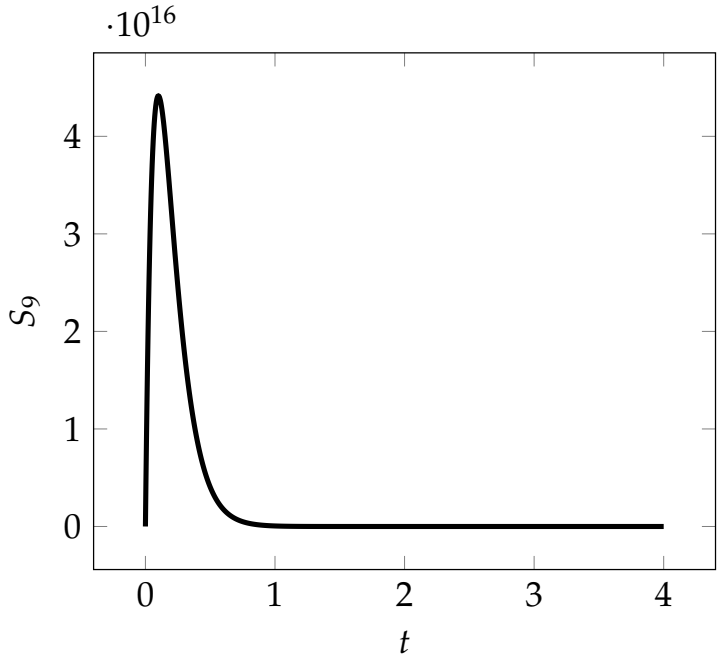


Figure 4.5: Source term used for velocity impulse point source applied to $z$-velocity

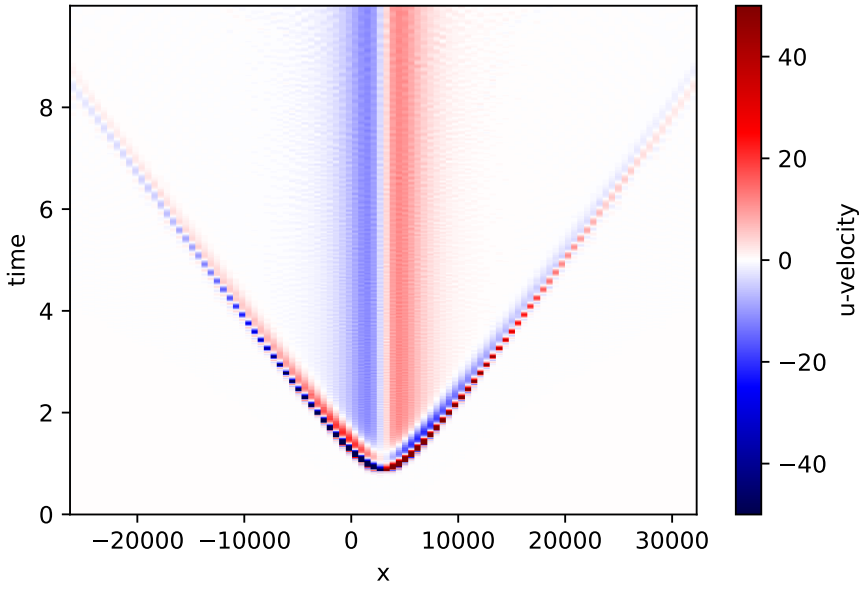


Figure 4.6: Space-time plot for wave produced by velocity impulse point source in acoustic media. We take a slice at $(3000, 3000, 20000)$ perpendicular to the $z$-axis and plot the $u$-velocity along $x$-axis at different times.

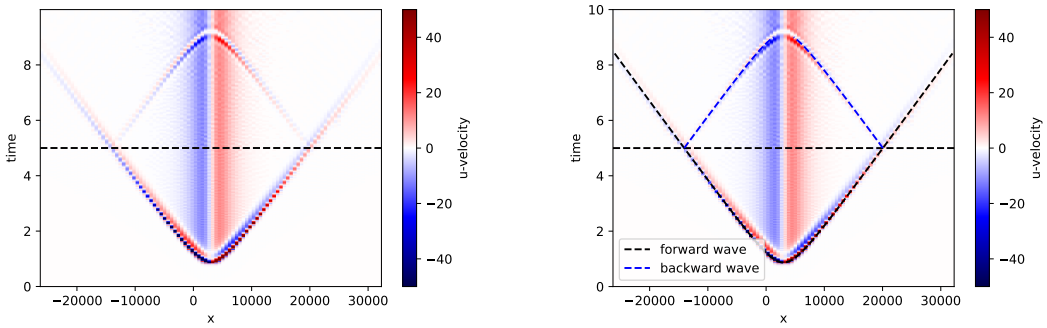


(a) Wave produced by velocity impulse in acoustic media with ITM

(b) Expected location of forward and reflected waves in time. The dashed lines denote the expected location of the wavefronts at given time.

Figure 4.7: Space-time plot for wave produced by velocity impulse point source in acoustic media with ITM. We take a slice at $(3000, 3000, 20000)$ perpendicular to the $z$-axis and plot the $u$-velocity along $x$-axis at different times.

This confirms our hypothesis that the reflected wave has the same speed as the forward going wave. This also confirms that the application of ITM produces a reflected wave successfully in acoustic media.

## 4.3 Time-reversal of waves created by a velocity impulse point source in elastic media

Here, we apply a velocity impulse point source like in section 4.2 but on an elastic medium. We choose the material parameters from the half-space of the benchmark case WP2-LOH1[1] to make it a homogenous elastic medium. The material parameters are characterized by

$$\begin{aligned} \rho &= 2700.0, \\ \mu &= 3.23980992 \cdot 10^{10}, \\ \lambda &= 3.24038016 \cdot 10^{10}, \end{aligned} \tag{4.6}$$

which makes the velocities of P- and S-waves to be

$$\begin{aligned} v_p &= 6000.0, \\ v_s &= 3464.0. \end{aligned} \tag{4.7}$$

In this case we extend our computational domain even further to $[-104000, 128000] \times [-104000, 128000] \times [0, 136000]$ and a simulation time of $t = 18.0$ with ITM applied at

[1] https://seissol.readthedocs.io/en/latest/pointsource.html

$t = 9.0$ such that the originating waves do not reflect back from the boundaries at the $x$- and $y$-axis ensuring that reflections due to the ITM are clearly noticeable. Our velocity impulse source is at $(12000, 12000, 68000)$, the center of the domain. We chose to analyse the simulation for a longer time in this scenario such that the S-wave reaches the slice. We choose an unstructured tetrahedral mesh with around 13 million elements similar to the acoustic case. We apply a source which has already been discussed in equation 4.5 and figure 4.5.

We pick a slice at $(12000, 12000, 40000)$ and visualise the wavefield with velocity in $x$-direction and the displacement along the $x$-axis. With this setup and velocity impulse, we see that the velocity in $x$-direction looks like in figure 4.8.

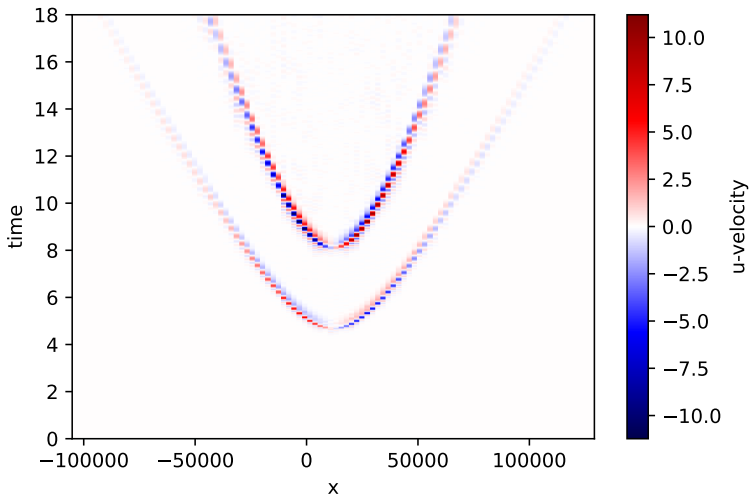


Figure 4.8: Space-time plot for waves produced by velocity impulse point source in elastic media. We take a slice at $(12000, 12000, 40000)$ perpendicular to the $z$-axis and plot the $u$-velocity along $x$-axis at different times.

We integrate the obtained velocity field to plot displacement field in $x$-direction as shown in figure 4.9.

We can clearly notice two propagating waves as expected as we are dealing with an elastic medium now. We notice a static displacement field in between the two waves. This is a common phenomenon in displacement fields built with simulation codes in seismic simulations. We now apply ITM on the same setup at $t = 9.0$. The wavefield with the application of the ITM looks like in figure 4.10.

We notice that there are two clearly reflected waves travelling back to the source. The faster moving wave i.e., P-wave leaves our slice around $t = 13.0$ which is around 4 seconds after the application of ITM which is the time it travelled through the slice just before the application of ITM. The slower moving wave, i.e., S-wave also has a reflection symmetric about line $t = 9.0$. We now plot the displacement plot in x-direction on the slice just like we did in figure 4.9 in figure 4.11.

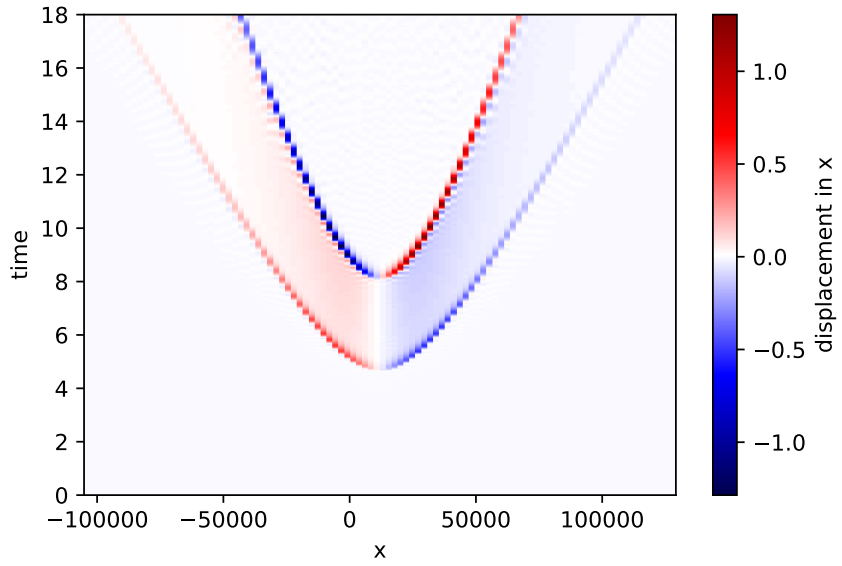


Figure 4.9: Space-time plot for waves produced by velocity impulse point source in elastic media. We take a slice at $(12000, 12000, 40000)$ perpendicular to the $z$-axis and plot the displacement in $x$-direction along $x$-axis at different times. We integrate the velocity field to obtain the displacement field.

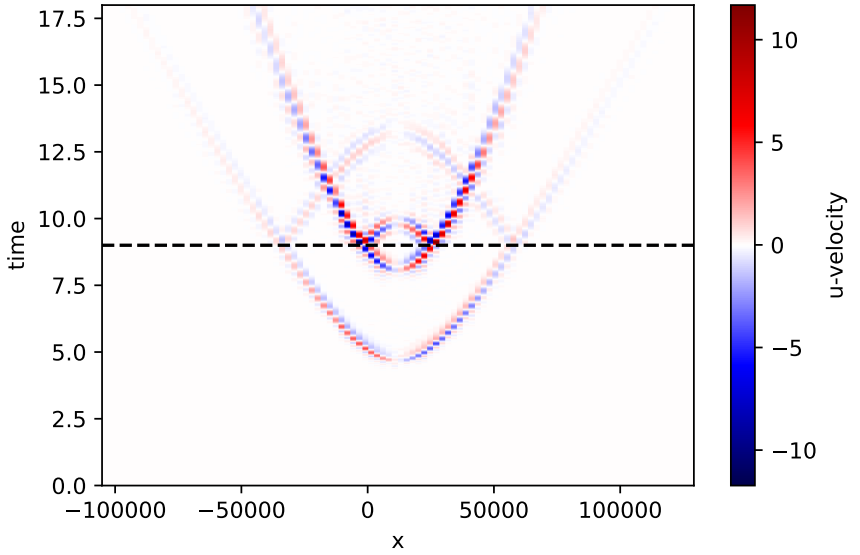


Figure 4.10: Space-time plot for waves produced by velocity impulse point source in elastic media with ITM. We take a slice at $(12000, 12000, 40000)$ perpendicular to the $z$-axis and plot the $u$-velocity along $x$-axis at different times.

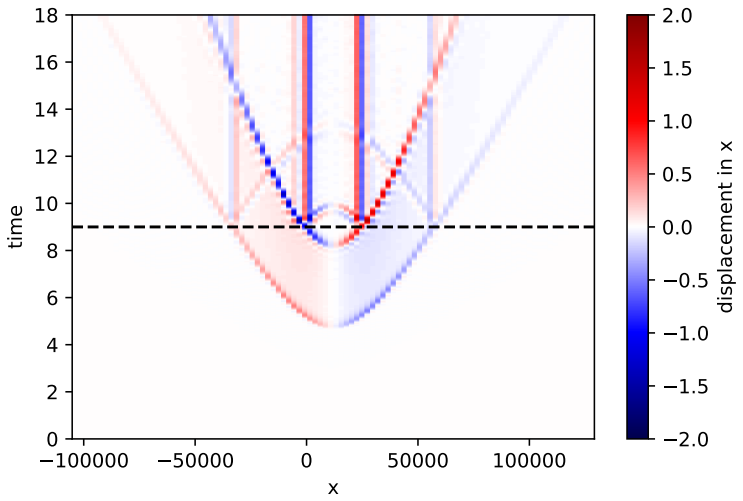


Figure 4.11: Space-time plot for waves produced by velocity impulse point source in elastic media with ITM. We take a slice at $(12000, 12000, 40000)$ perpendicular to the $z$-axis and plot the displacement in $x$-direction along the $x$-axis at different times. We integrate the velocity field to obtain the displacement field.

We see two reflections even in case of the displacement wavefield too and the static displacements between the two waves persist. But we see extra features here in case of the displacement wavefield. We obtain extra static displacements in time as vertical streaks which originate from the point where the waves meet the slice at ITM. These are not yet explained but we suspect they may be explained either by the physical phemonenon or due to the numerical implementation or due to errors produced to numerical integration of the velocity wavefields.

This shows that both the waves can be reflected simultaneously by scaling the material parameters to change their impedance to obtain a component which is reflected back to its source.

## 4.4 Time-reversal of P-wave created by a velocity impulse point source in elastic media

We now demonstrate the reflection of just the P-wave by scaling the Lamé parameter $\lambda$ and keeping the second Lamé parameter $\mu$ constant.

The same setup is used as in section 4.3 and we try to reflect just the P-wave while letting the S-wave travel unaffected in time. The slice and everything else about the simulation setup remain the same. The wavefields without ITM are given in figures 4.8 and 4.9

After the application of the ITM, we see a reflection in the wavefield in figure 4.12. As the reflection in figure 4.12 is visible but is faint, we plot the same with a different colorbar just to show the reflection in a clearer way as depicted in figure 4.13

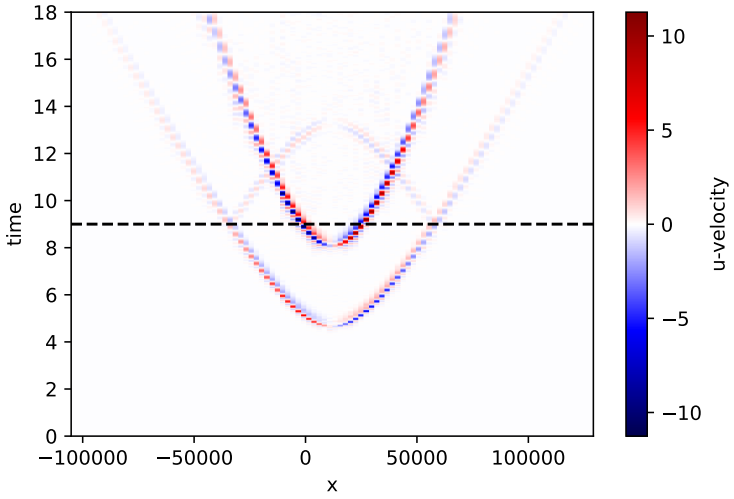


Figure 4.12: Reflection of P-wave in elastic Media with ITM. We take a slice at $(12000, 12000, 40000)$ perpendicular to the $z$-axis and plot the $u$-velocity along the $x$-axis at different times.

We can clearly see here in this plot that there is a P-wave which is reflected without affecting the S-wave. This provides us a proof of concept where we can reflect one wave by changing its impedance while maintaining the other wave's impedance constant.

We plot the displacement wavefield in figure 4.14 and we can see the reflected P-wave in displacement wavefield and the static displacement is noticed in this case too just like in the case of reflecting both the waves.

## 4.5 Time-reversal of S-wave created by a velocity impulse point source in elastic media

In this section, we demonstrate the reflection of just the S-wave by modifying the Lamé parameters such that P-wave does not get reflected but the S-wave does. The same setup is used as in section 4.3. The wavefields without ITM are given in figures in 4.8 and 4.9.

After the application of the ITM, we see reflections in the wavefield in figure 4.15 showing the zoomed version near the ITM so that the reflected part is clearly visible in figure 4.15b.

We plot the displacement wavefield in figure 4.16 and we can see the reflected S-wave in displacement wavefield and the static displacement like in previous section persists. We need more investigation into this to understand this static displacement.

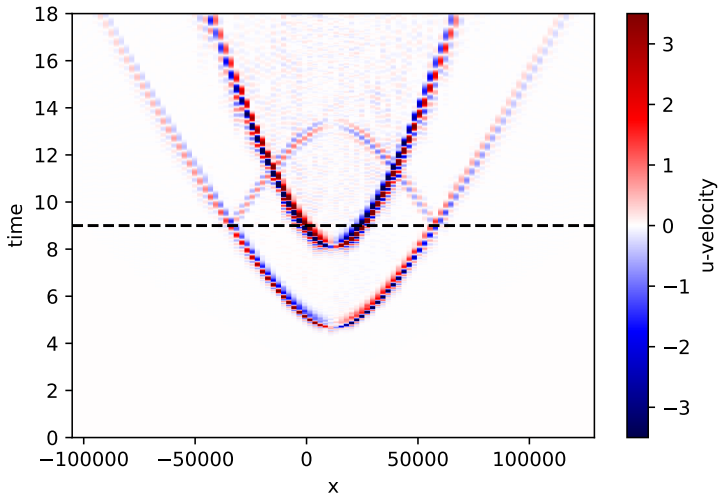


Figure 4.13: Reflection of P-wave in elastic media with ITM. We take a slice at $(12000, 12000, 40000)$ perpendicular to the $z$-axis and plot the $u$-velocity along the $x$-axis at different times. We use a different colorbar from figure 4.12 to show the reflection more clearly.

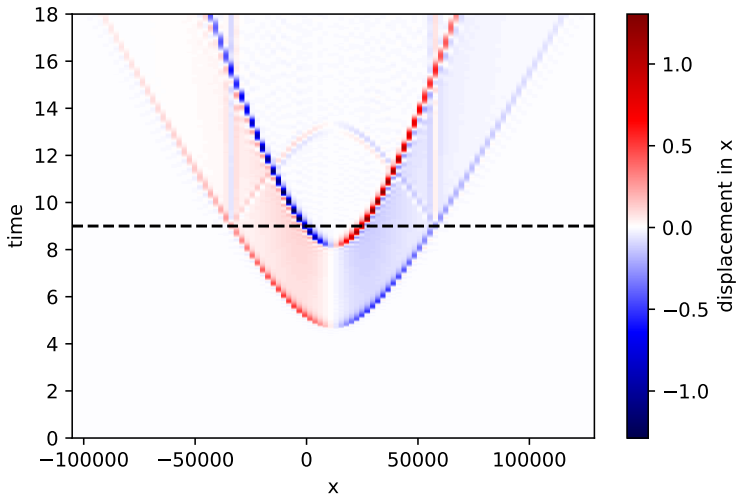


Figure 4.14: Reflection of P-wave in elastic media with ITM. We take a slice at $(12000, 12000, 40000)$ perpendicular to the $z$-axis and plot the displacement in $x$-direction along the $x$-axis at different times. We integrate the velocity field to obtain the displacement field.

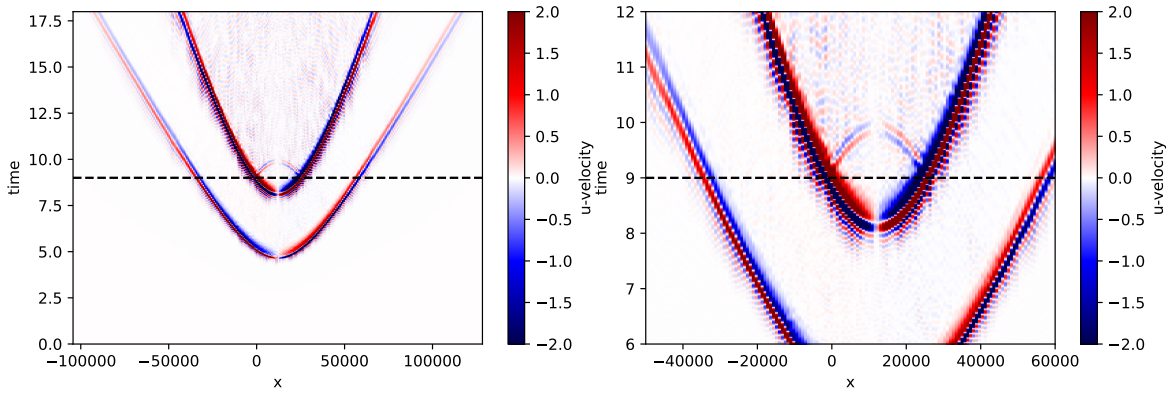


(a) Reflecting S-wave in elastic media. We take a slice at $(12000, 12000, 40000)$ perpendicular to the $z$-axis and plot the $u$-velocity along the $x$-axis at different times.

(b) Zoomed cut section of figure 4.15a to show the reflected S-wave more clearly.

Figure 4.15: Reflection of S-wave in elastic media with ITM. We take a slice at $(12000, 12000, 40000)$ perpendicular to the $z$-axis and plot the $u$-velocity along the $x$-axis at different times.

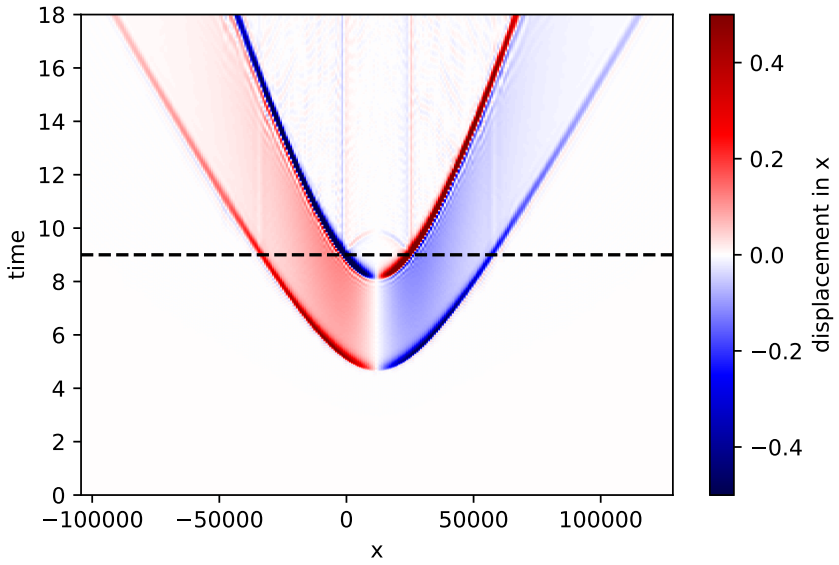


Figure 4.16: Reflection of S-wave in elastic media with ITM. We take a slice at $(12000, 12000, 40000)$ perpendicular to the $z$-axis and plot the displacement in $x$-direction along the $x$-axis at different times. We integrate the velocity field numerically to obtain the displacement field.

We see here in figure 4.15 that there is a S-wave which is reflected without affecting the P-wave. This provides us a proof of concept where we show that we can reflect one wave by changing its impedance while maintaining the other wave's impedance constant.

## 4.6 Time-reversal of wave created by a pressure impulse point source in acoustic media

We choose the same material and mesh as in section 4.2 and change the source term to a pressure impulse. A pressure impulse source term is a moment tensor with all non-diagonal elements zero and equal diagonal elements [She19, Cha. 9]. These are applied to the first three equations of the set of equations 2.14. An exponentially decaying source is chosen similar to the source in section 4.2. With this setup, the normal propagation of the wave looks at a slice which is already explained in section 4.2 like in figure 4.17.

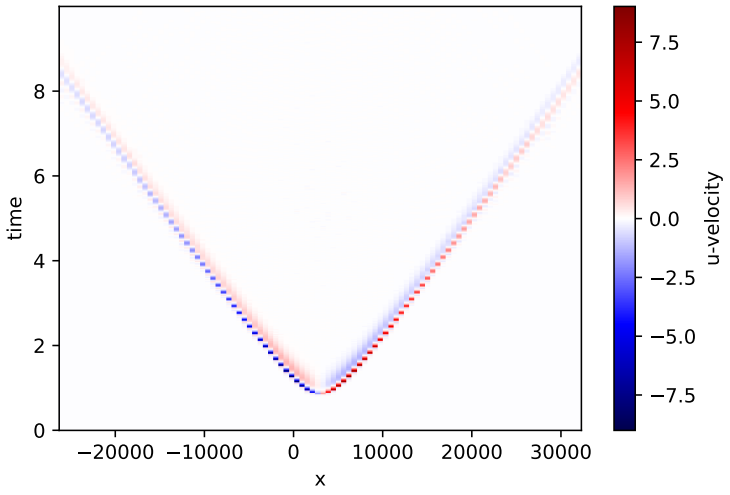


Figure 4.17: Space-time plot for wave produced by pressure impulse point source in acoustic media. We take a slice at $(3000, 3000, 20000)$ perpendicular to the $z$-axis and plot the $u$-velocity along the $x$-axis at different times.

We notice that we have only one wave propagating in time as expected as we have an acoustic medium and it reaches our slice around $t = 1.5$. We now apply ITM at $t = 5.0$ and the wavefield looks like in figure 4.18.

We notice that there is a reflected wave travelling back to the source. The reflected wave leaves our slice around $t = 8.5$, showing that the reflected wave is reflected along the line $t = 5.0$, which is our point in time when we applied the ITM. This confirms that the application of ITM produces a reflected wave successfully in acoustic media even when the waves are created by pressure impulse point sources.

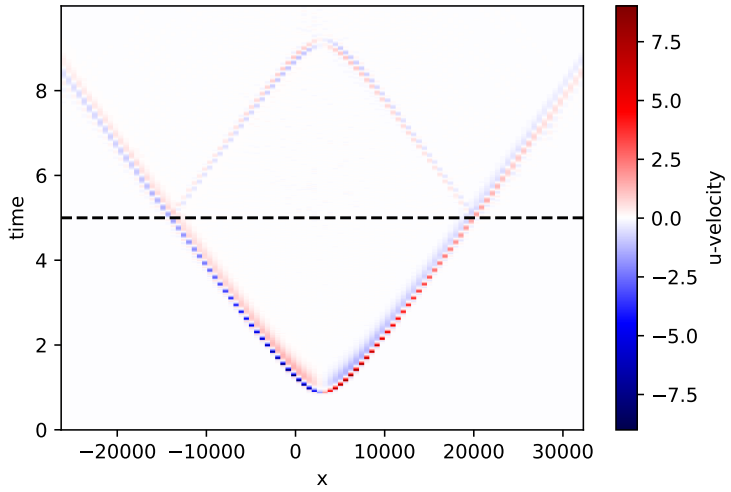


Figure 4.18: Space-time plot for wave produced by pressure impulse point source in acoustic media with ITM. We take a slice at $(3000, 3000, 20000)$perpendicular to the $z$-axis and plot the $u$-velocity along the $x$-axis at different times.

## 4.7 Time-reversal of waves created by a force couple moment tensor in elastic media

We now apply a force couple moment tensor as a source term in an elastic medium. [She19, Sec. 9.2] defines a force couple moment tensor as

$$\mathbf{M} = \begin{bmatrix} M_{11} & M_{12} & M_{13} \\ M_{21} & M_{22} & M_{23} \\ M_{31} & M_{32} & M_{33} \end{bmatrix}, \tag{4.8}$$

where $M_{ij}$ is a pair of opposing forces pointing in $i$-direction, separated in the $j$-direction. The condition that angular momentum is conserved requires that $M_{ij} = M_{ji}$. As a consequence, $\mathbf{M}$ has only six independent elements. The moment tensor is applied to the first six equations of the set of equations 2.14 as per the direction it is to be applied [KMD07].

### 4.7.1 Moment tensor with non-diagonal elements zero

We begin with a moment tensor which has only diagonal elements not equal to each other. The material parameters and simulation setup are the same as in section 4.3. The moment tensor chosen is

$$\mathbf{M} = \begin{bmatrix} 0.9 & 0.0 & 0.0 \\ 0.0 & 0.1 & 0.0 \\ 0.0 & 0.0 & -0.1 \end{bmatrix} \times 10^{19}. \tag{4.9}$$

With this setup, the space-time plot at the slice chosen looks as shown in figure 4.19.

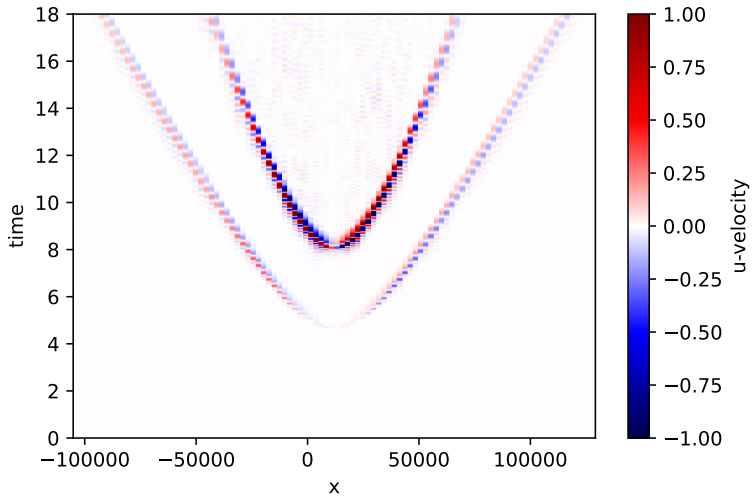


Figure 4.19: Space-time plot for waves produced by force couple moment tensor with non-diagonal elements zero in elastic media. We take a slice at $(12000, 12000, 40000)$ perpendicular to the $z$-axis and plot the $u$-velocity along the $x$-axis at different times.

We now apply ITM at $t = 9.0$ and notice that both the waves are reflected as expected in figure 4.20.

As expected, there are two reflections in the wavefield. This confirms that ITM could be used to obtain a reversed wave in case of waves generated by a force couple moment tensor.

### 4.7.2 Moment tensor with non-diagonal elements non-zero

We now use a moment tensor obtained from a seismic event that occured near Tori Shima, Japan [Kan+93], [She19]. To obtain stable results, the isotropic component is constrained to zero as

$$\mathbf{M} = \begin{bmatrix} -1.8 & -0.38 & -0.96 \\ -0.38 & -1.9 & 0.62 \\ -0.96 & 0.62 & 3.7 \end{bmatrix} \times 10^{17}. \tag{4.10}$$

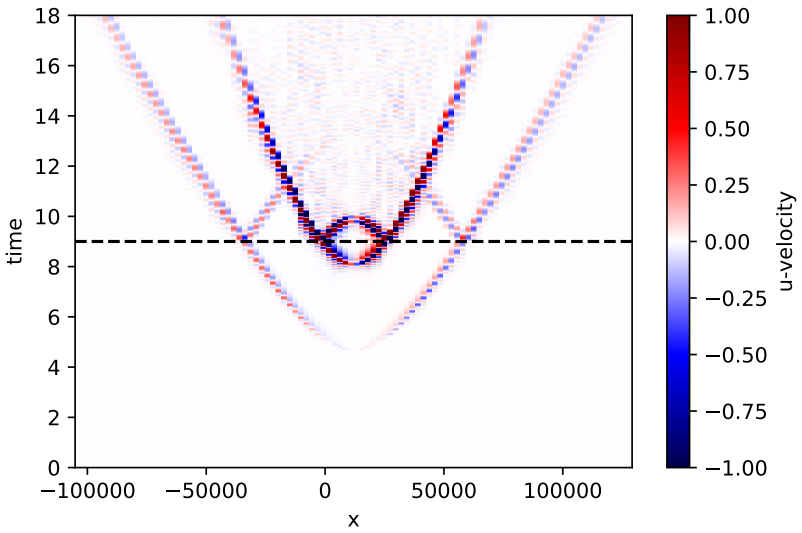


Figure 4.20: Space-time plot for waves produced by force couple moment tensor with non-diagonal elements zero in elastic media with ITM. We take a slice at $(12000, 12000, 40000)$ perpendicular to the $z$-axis and plot the $u$-velocity along the $x$-axis at different times.

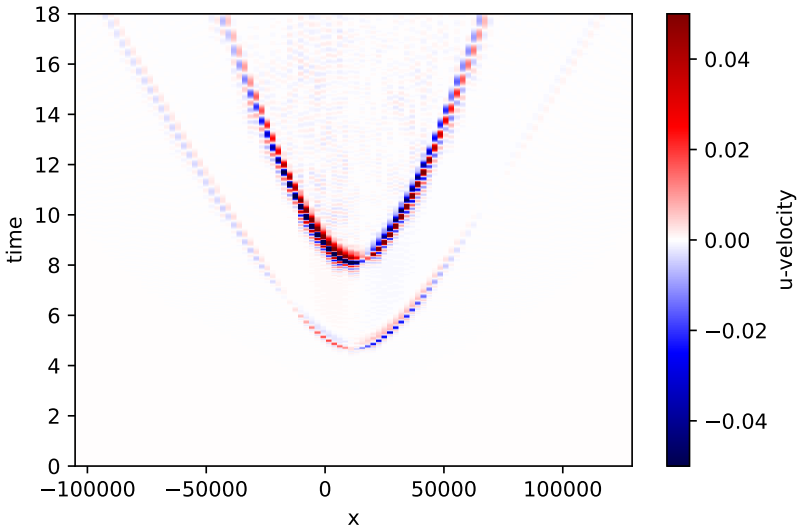


Figure 4.21: Space-time plot for waves produced by force couple moment tensor with non-diagonal elements in elastic media. We take a slice at $(12000, 12000, 40000)$ perpendicular to the $z$-axis and plot the $u$-velocity along the $x$-axis at different times.

With this setup, the space-time plot at the slice chosen looks as shown in figure 4.21.

We now apply ITM at $t = 9.0$ and notice that both the waves are reflected as expected in figure 4.22.

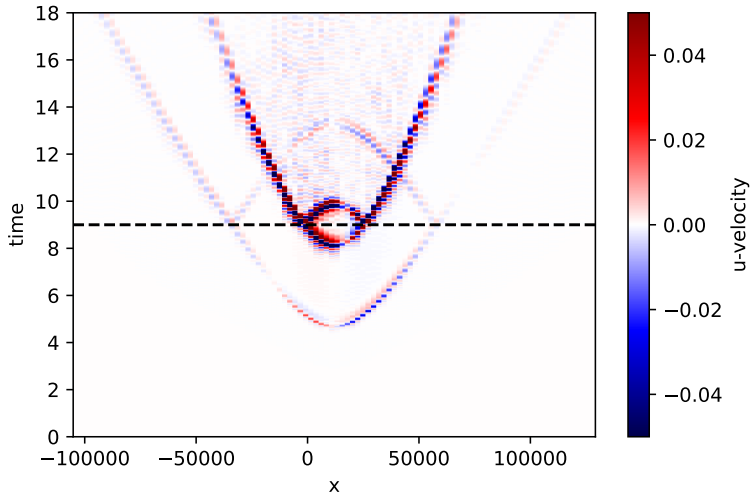


Figure 4.22: Space-time plot for waves produced by force couple moment tensor with non-diagonal elements in elastic media with ITM. We take a slice at $(12000, 12000, 40000)$ perpendicular to the $z$-axis and plot the $u$-velocity along the $x$-axis at different times.

As expected, there are two reflections in the wavefield. This confirms that ITM could be used to obtain a reversed wave in case of waves generated by a force couple moment tensor even when there are non-zero non diagonal elements.

## 4.8 Convergence Test

We now perform a convergence test to verify that our ITM implementation is accurate and converges with our ADER-DG scheme. We check the error between our numerical implementation and the analytical solution developed in section 3.3. The mesh is setup with equal triangular elements on a cubic domain of $[-1, 1] \times [-1, 1] \times [-1, 1]$ with the number of elements in each direction varying in $[4, 8, 16, 32, 64, 128]$. We calculate the $L^2$ error of $u$-velocity of the solution with respect to the analytical solution as per section 3.3. We calculate this error for different polynomial orders within $[1, 2, 3, 4, 5]$ used in the reference element of the DG scheme. We expect a convergence order of $p + 1$ where $p$ is the polynomial order used in the DG scheme used [CKS11]. We now plot the $L^2$ error norm of $u$-velocity in figure 4.23.

We notice that the slope of the curve increases as expected with increasing order of the polynomial. In case of order 5, there is a slight increase of error for grid size 128.

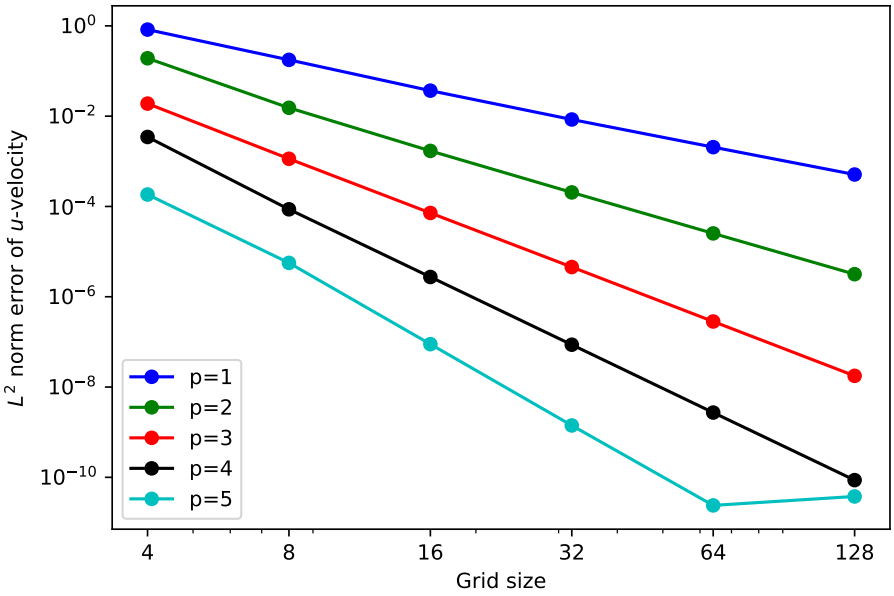


Figure 4.23: Convergence plot for $L^2$ norm of $u$-velocity for acoustic travelling wave with ITM. The error is calculated with respect to the analytical solution in section 3.3.

This is suspected to be due to the error plateauing as the precision hits the floating point precision. We perform a linear fit on the log-log plot to get a slope such that we can check the convergence order of the plot. We remove the last point from the fit for $p = 5$ as it is suspected to be an outlier. We get the following convergence orders for different polynomial orders shown in table 4.1 and figure 4.24.

Table 4.1: Convergence order vs polynomial order obtained from the convergence study of acoustic travelling wave with ITM

| **Polynomial Order** | **Convergence Order** |
|---|---|
| 1 | 2.13 |
| 2 | 3.15 |
| 3 | 4.00 |
| 4 | 5.03 |
| 5 | 5.77 |

We now plot the expected error with the expected convergence order vs the actual error during the simulations in figure 4.25.

We notice that our numerical error agrees with the expected theoretical error well. This concludes the correctness of our implementation of ITM in SeisSol with ADER-DG.

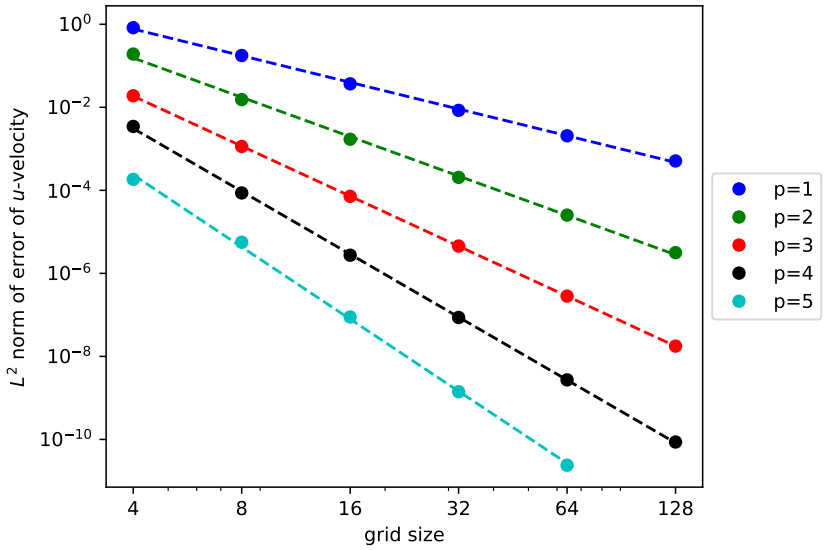


Figure 4.24: Linear fit of $\log(L^2)$ and $\log(gridsize)$ plot for acoustic travelling wave with ITM. Dashed lines denote the linear fit of the logarithms. The slope of the dashed lines denotes the obtained convergence order. The outlier for $p = 5$ is removed from the fit.

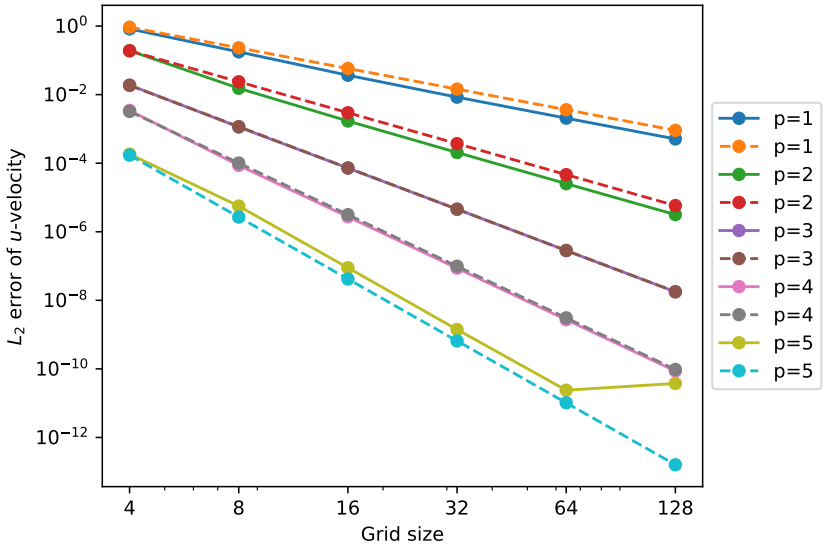


Figure 4.25: Expected $L^2$ norm vs actual $L^2$ norm for acoustic travelling wave with ITM. Solid lines denote the original error where as the dashed lines are the expected error. The expected error is calculated with the expected convergence order as the slope and the mean of logarithms of errors as the intercept of the line.

## 4.9 Discussion

In this chapter, we looked at the results obtained from applying the ITM on seismic waves. We began with the reflection of a travelling planar wave in acoustic media and then moved on to spherical waves generated by a velocity impulse point source in acoustic and elastic media. We then looked at the reflection of just the P-wave and S-wave separately to show that we can reflect just one wave by changing its impedance while keeping the other wave's impedance constant. In the end, we ran a convergence study of our implementation with the analytical solution obtain in section 3.3 to conclude that our implementation is convergent with the expected convergence order.

# 5 Conclusion and Future Research Outlook

In this thesis, we implemented and analysed the wavefield reversal method ITM in the numerical simulation software SeisSol. We first presented the basic theory of elastic wave propagation and the numerical ADER-DG scheme used in SeisSol in chapter 2. We then presented the theoretical foundation of the ITM method in chapter 3, the expected solutions for a simple one dimensional case in section 3.2 and the wavefield reversal for a three dimensional wave in acoustic medium in section 3.3. The energy behaviour of the ITM method was analysed for different phases of the ITM. We then presented the implementation details of the ITM method in SeisSol in section 3.4. The implementation details for different wave reversal scenarios were discussed in sections 3.4.1, 3.4.2, 3.4.3, 3.4.4 and the required modifications for the time step size were discussed in section 3.4.5.

Finally, we presented the results of various studies conducted to analyse the effects of different scenarios on the wavefield reversal in chapter 4. We first reverse a planar acoustic wave in a homogeneous medium in section 4.1 and analyse the reversal to verify that the reversed and forward waves have identical speeds as expected from the analytical soutions. We later reverse spherical waves generated by point sources in WP2-LOH1 case, modified to make the medium homogeneous, in acoustic and elastic media in sections 4.2 and 4.3. We verify that the reversal of just one wave is possible while letting the other wave stay forward propagating in sections 4.4 and 4.5. We then verify that our implementation in SeisSol is converging by verifying the numerical results with the analytical solutions developed is increased in section 4.8. We notice that the numerical results are converging faster to the analytical solutions as the polynomial order of the DG scheme increases. This verifies that the ITM method proposed by [Bac+16] on waterwaves can be applied analogously on seismic waves to obtain a reversed component retracing them to the source.

Currently, the ITM parameters are heuristically determined. As part of future research, analytical solutions for the spherical waves produced by point sources may be calculated to select the appropriate parameters for ITM. More complex scenarios and wavefield reversal in heterogeneous media can be studied. The ITM method may be used to study the effects of different wave propagation properties on the wavefield reversal. ITM approach and its implementation for other scenarios like anisotropic, viscoelastic and poroelastic media can be studied. Noise in the simulation data obtained during the reversal process could be filtered out to obtain a clearer refocusing pattern and more accurate analysis in the phase shift could be performed.

# Abbreviations

**TRM** Time Reversal Mirror

**ITM** Instantaneous Time Mirror

**DG** Discontinuous Galerkin

**ADER** Arbitrary high-order schemes using DERivates

**DG-FE** Discontinuous Galerkin Finite Element

**RK-DG** Runge Kutta Discontinuous Galerkin

**CFL** Courant-Friedrichs-Lewy

**LTS** Local Time Stepping

**PDE** Partial Differential Equation

# List of Figures

# List of Tables

# Bibliography


[AR02] K. Aki and P. G. Richards. *Quantitative Seismology*. 2nd. University Science Books, 2002. ISBN: 0935702962.

[Bac+16] V. Bacot, M. Labousse, A. Eddi, M. Fink, and E. Fort. "Time reversal and holography with spacetime transformations." In: *Nature Physics* 12.10 (Oct. 2016), pp. 972–977. ISSN: 1745-2481. DOI: 10.1038/nphys3810.

[Bre15] A. N. Breuer. "High Performance Earthquake Simulations." PhD thesis. Technische Universität München: Lehrstuhl für Informatik mit Schwerpunkt Wissenschaftliches Rechnen, 2015.

[But87] J. C. Butcher. *The Numerical Analysis of Ordinary Differential Equations: Runge-Kutta and General Linear Methods*. USA: Wiley-Interscience, 1987. ISBN: 0471910465.

[Cat+08] S. Catheline, N. Benech, J. Brum, and C. Negreira. "Time Reversal of Elastic Waves in Soft Solids." In: *Phys. Rev. Lett.* 100 (6 Feb. 2008), p. 064301. DOI: 10.1103/PhysRevLett.100.064301.

[CKS11] B. Cockburn, G. E. Karniadakis, and C.-W. Shu. *Discontinuous Galerkin Methods: Theory, Computation and Applications*. 1st. Springer Publishing Company, Incorporated, 2011. ISBN: 3642640982.

[CKT09] M. Castro, M. Käser, and E. F. Toro. "Space–time adaptive numerical methods for geophysical applications." In: *Philosophical Transactions of the Royal Society of London A: Mathematical, Physical and Engineering Sciences* (2009).

[Cui+10] Y. Cui, K. Olsen, T. Jordan, K. Lee, J. Zhou, P. Small, D. Roten, G. Ely, D. Panda, A. Chourasia, J. Levesque, S. Day, and P. Maechling. "Scalable Earthquake Simulation on Petascale Supercomputers." In: Nov. 2010, pp. 1–20. DOI: 10.1109/SC.2010.45.

[DK06] M. Dumbser and M. Käser. "An arbitrary high-order discontinuous Galerkin method for elastic waves on unstructured meshes — II. The three-dimensional isotropic case." In: *Geophysical Journal International* 167.1 (Oct. 2006), pp. 319–336. ISSN: 0956-540X. DOI: 10.1111/j.1365-246X.2006.03120.x.

[DKT07] M. Dumbser, M. Käser, and E. F. Toro. "An arbitrary high-order Discontinuous Galerkin method for elastic waves on unstructured meshes - V. Local time stepping and p-adaptivity." In: *Geophysical Journal International* (2007).

[DM05] M. Dumbser and C.-D. Munz. "ADER Discontinuous Galerkin Schemes for Aeroacoustics." In: *Comptes Rendus Mécanique* 333 (2005), pp. 683–. DOI: 10.1016/j.crme.2005.07.008.

[DM06] M. Dumbser and C.-D. Munz. "Building Blocks for High Order Discontinuous Galerkin Schemes." In: *Journal of Scientific Computing* 27.1 (2006), pp. 215–230. ISSN: 1573-7691. DOI: 10.1007/s10915-005-9025-0.

[Dum03] M. Dumbser. "On the Improvement of Efficiency and Storage Requirements of the Discontinuous Galerkin Method for Aeroacoustics." In: *PAMM* 3.1 (2003), pp. 426–427. DOI: https://doi.org/10.1002/pamm.200310484.

[FF17] M. Fink and E. Fort. "From the time-reversal mirror to the instantaneous time mirror." In: *The European Physical Journal Special Topics* 226.7 (May 2017), pp. 1477–1486. ISSN: 1951-6401. DOI: 10.1140/epjst/e2016-60258-8.

[Fin+89] M. Fink, C. Prada, F. Wu, and D. Cassereau. "Self focusing in inhomogeneous media with time reversal acoustic mirrors." In: *Proceedings., IEEE Ultrasonics Symposium,* 1989, 681–686 vol.2. DOI: 10.1109/ULTSYM.1989.67072.

[Fin97] M. Fink. "Time Reversed Acoustics." In: *Physics Today* 50.3 (Mar. 1997), pp. 34–40. ISSN: 0031-9228. DOI: 10.1063/1.881692. eprint: https://pubs.aip.org/physicstoday/article-pdf/50/3/34/10961392/34_1_online.pdf.

[GLM08] G. Gassner, F. Lörcher, and C.-D. Munz. "A Discontinuous Galerkin Scheme based on a Space-Time Expansion II. Viscous Flow Equations in Multi Dimensions." In: *Journal of Scientific Computing* 34.3 (Mar. 2008), pp. 260–286. ISSN: 1573-7691. DOI: 10.1007/s10915-007-9169-1.

[Kan+93] H. Kanamori, G. Ekström, A. Dziewonski, J. Barker, and S. Sipkin. "Seismic Radiation by Magma Injection: An Anomalous Seismic Event Near Tori Shima, Japan." In: *Journal of Geophysical Research* 98 (Apr. 1993), pp. 6511–6522. DOI: 10.1029/92JB02867.

[Käs+10] M. Käser, C. Castro, V. Hermann, and C. Pelties. "SeisSol – A Software for Seismic Wave Propagation Simulations." In: *High Performance Computing in Science and Engineering, Garching/Munich 2009*. Ed. by S. Wagner, M. Steinmetz, A. Bode, and M. M. Müller. Berlin, Heidelberg: Springer Berlin Heidelberg, 2010, pp. 281–292. ISBN: 978-3-642-13872-0.

[KD06] M. Käser and M. Dumbser. "An arbitrary high-order discontinuous Galerkin method for elastic waves on unstructured meshes — I. The two-dimensional isotropic case with external source terms." In: *Geophysical Journal International* 166.2 (Aug. 2006), pp. 855–877. ISSN: 0956-540X. DOI: 10.1111/j.1365-246X.2006.03051.x.

[KGN21] D. A. Kopriva, G. J. Gassner, and J. Nordström. "Stability of Discontinuous Galerkin Spectral Element Schemes for Wave Propagation when the Coefficient Matrices have Jumps." In: *Journal of Scientific Computing* 88.1 (2021), p. 3. DOI: 10.1007/s10915-021-01516-w.

[KL05] A. Kaufman and A. L. Levshin. *Acoustic and Elastic Wave Fields in Geophysics, III*. 3rd. Elsevier, 2005. ISBN: 0444519556.

[KMD07] M. Käser, P. M. Mai, and M. Dumbser. "Accurate Calculation of Fault-Rupture Models Using the High-Order Discontinuous Galerkin Method on Tetrahedral Meshes." In: *Bulletin of the Seismological Society of America* 97.5 (Oct. 2007), pp. 1570–1586. ISSN: 0037-1106. DOI: 10.1785/0120060253.

[LeV02] R. J. LeVeque. *Finite Volume Methods for Hyperbolic Problems*. Cambridge Texts in Applied Mathematics. Cambridge University Press, 2002. DOI: 10.1017/CBO9780511791253.

[Rie+15] M. Rietmann, D. Peter, O. Schenk, B. Uçar, and M. Grote. "Load-Balanced Local Time Stepping for Large-Scale Wave Propagation." In: *Parallel and Distributed Processing Symposium (IPDPS), 2015 IEEE International*. IEEE. 2015.

[Sch+09] M. Schlegel, O. Knoth, M. Arnold, and R. Wolke. "Multirate Runge–Kutta schemes for advection equations." In: *Journal of Computational and Applied Mathematics* 226.2 (2009). Special Issue: Large scale scientific computations, pp. 345–357. ISSN: 0377-0427. DOI: https://doi.org/10.1016/j.cam.2008.08.009.

[Sen+14] B. Seny, J. Lambrechts, T. Toulorge, V. Legat, and J.-F. Remacle. "An efficient parallel implementation of explicit multirate Runge-Kutta schemes for discontinuous Galerkin computations." In: *Journal of Computational Physics* (2014).

[She19] P. M. Shearer. *Introduction to Seismology*. 3rd ed. Cambridge University Press, 2019. DOI: 10.1017/9781316877111.

[The] The Sage Developers. *SageMath, the Sage Mathematics Software System (Version 10.1.0)*. URL: https://www.sagemath.org.

[TMN01] E. F. Toro, R. C. Millington, and L. A. M. Nejad. "Towards Very High Order Godunov Schemes." In: *Godunov Methods: Theory and Applications*. Ed. by E. F. Toro. New York, NY: Springer US, 2001, pp. 907–940. ISBN: 978-1-4615-0663-8. DOI: 10.1007/978-1-4615-0663-8_87.

[Wei16] F. Weinert. "Loschmidt's Demon: Reversibility and Irreversibility." In: *The Demons of Science: What They Can and Cannot Tell Us About Our World*. Cham: Springer International Publishing, 2016, pp. 127–130. ISBN: 978-3-319-31708-3. DOI: 10.1007/978-3-319-31708-3_16.

[WK14] A. Winters and D. Kopriva. "High-Order Local Time Stepping on Moving DG Spectral Element Meshes." In: *Journal of Scientific Computing* 58 (Jan. 2014). DOI: 10.1007/s10915-013-9730-z.